J. Fluid Mech. (2018), *vol.* 843, *pp.* 382–418. © Cambridge University Press 2018
doi:10.1017/jfm.2018.125

A Kármán–Howarth–Monin equation for variable-density turbulence

Chris C. K. Lai[1,†], **John J. Charonko**[1] **and Katherine Prestridge**[1]

[1]Physics Division, Los Alamos National Laboratory, Los Alamos, NM 87545, USA

(Received 3 August 2017; revised 9 January 2018; accepted 25 January 2018;
first published online 27 March 2018)

We present a generalisation of the Kármán–Howarth–Monin (K–H–M) equation to include variable-density (VD) effects. The derived equation (i) reduces to the original K–H–M equation when density is a constant and (ii) leads to a VD analogue of the 4/5-law with the same value of constant (=4/5) appearing as the prefactor of the dissipation rate. The equation is employed to understand negative turbulent kinetic energy production in a SF_6 turbulent round jet with an initial density ratio of 4.2. From a Reynolds-averaged Navier–Stokes (RANS) perspective, negative production means that the mean flow is strengthened at the expense of the energy of turbulent fluctuations. We show that the associated energy transfer is accomplished by the deformation of smaller turbulent eddies into large ones in the development region of the jet and is captured by the linear scale-by-scale energy transfer term in the VD K–H–M equation. The nonlinear transfer term of the VD K–H–M equation depicts a conventional forward cascade for all eddies having a size less than the Eulerian integral length scale, regardless of their orientation. The net effect is a retarded energy cascade in the non-Boussinesq jet that has not been accounted for by existing turbulence theories. Implications of this observation for turbulence modelling are discussed.

Key words: jets, turbulence theory, turbulent mixing

1. Introduction

The notion of an energy cascade is fundamental in existing theories and predictive models of turbulent flows (Pope 2000). For constant-density flows, the Richardson–Kolmogorov phenomenology has been postulated to hold in high-Reynolds-number, locally homogeneous and locally isotropic flows under the ansatz of Kolmogorov's 1941 theory. A well-known prediction of the theory is the so-called Kolmogorov 4/5-law, which is one of the few exact relations derivable from the Navier–Stokes equations. The law is valid for turbulent scales within the inertial subrange and describes a scale-invariant energy transfer from large to small scales (a forward cascade). The turbulent dissipation rate, $\overline{\epsilon}$, is used as a surrogate for the interscale

†Email address for correspondence: chrislck@lanl.gov

https://doi.org/10.1017/jfm.2018.125 Published online by Cambridge University Press

energy transfer rate Π ($\overline{\epsilon} \approx -\Pi$) in turbulence modelling approaches such as Reynolds-averaged Navier–Stokes (RANS) and large-eddy simulation (LES). The 4/5-law is only a function of eddy sizes, the 'scale space' that links interscale energy transfer to dissipation at each physical spatial point. In flows lacking sufficient separation of scales, inhomogeneities and anisotropy are present, and a generalised 4/5-law known as the Kármán–Howarth–Monin (K–H–M) equation applies. The origin of the K–H–M equation began with the seminal paper by von Kàrmàn & Howarth (1938), who derived the equation for homogeneous isotropic turbulence. A more recent account of the full K–H–M equation is found in Hill (2002), where several exact relationships of the second-order velocity structure function are given.

The K–H–M equation describes the transfer of energy in both scale and physical space, with the latter reflecting the spatial development of the underlying flow. Several classes of turbulent flow have been studied using the equation. Casciola *et al.* (2003) analysed intermittency correction of velocity structure functions in shear turbulence using direct numerical simulation (DNS). In Gualtieri *et al.* (2007), the K–H–M approach was used to establish the necessary conditions that the filter scale of a large-eddy simulation must satisfy in order to achieve preservation of statistical properties of the resolved field in homogeneous shear flows. Marati, Casciola & Piva (2004) investigated the energetics of wall turbulence using a DNS dataset and laid down a complete and formally precise description of the dynamics of turbulence in the different regions of the channel flow. Valente & Vassilicos (2015) looked into the energy cascade in grid-generated non-equilibrium decaying turbulence and demonstrated that the appearance of a $-5/3$ power law scaling of the wavenumber or frequency in energy spectra does not necessarily imply a classic Richardson–Kolmogorov cascade. In a follow-up paper, Gomes-Fernandes, Ganapathisubramani & Vassilicos (2015) provided further evidence for this observation by showing that an inverse cascade exists in the production region behind a fractal grid in spite of a well-defined $-5/3$ power law over one decade in the streamwise fluctuating velocity spectrum. Further support for this observation is provided by the recent DNS study in the very-near-wake region of a two-dimensional square prism by Alves Portela, Papadakis & Vassilicos (2017). The scale-by-scale energy budgets in wakes and jets have been reported in Thiesset, Antonia & Danaila (2013) and Danaila, Antonia & Burattini (2004) respectively.

A number of experiments have reported observations that are at odds with the Richardson–Kolmogorov formulation because they could imply inverse energy cascades; the word 'could' is used because in constant-density flows there are two different physical mechanisms capable of transferring energy upscale. The energy cascade is one of them and the distortion of eddies by mean flow gradients is the other one. A detailed description of these two mechanisms is given in the next section. Chen, Meneveau & Katz (2006) reported positive mean subgrid-scale dissipation in homogeneous isotropic turbulence subjected to rapid straining–relaxation–destraining cycles; this feature was also observed in a subsequent DNS of the same flow performed by Gualtieri & Meneveau (2010). Multiple experiments have observed negative turbulent kinetic energy (t.k.e.) production, such as those of Liberzon *et al.* (2005) in a rapidly sheared flow near a solid boundary and in a Rayleigh–Bénard convection cell, and Charonko & Prestridge (2017) in a turbulent dense jet in coflow. While backscattering of energy is known to occur instantaneously in turbulent flows (Meneveau & Katz 2000) exhibiting a conventional forward cascade, in these experiments, a net transfer of energy from the fluctuations to the mean flow has occurred in the average sense and therefore poses challenges to modelling.

https://doi.org/10.1017/jfm.2018.125 Published online by Cambridge University Press

For instance, to model an inverse cascade, a negative turbulent viscosity would be required, and that could cause numerical instabilities. A better physical understanding of the interscale energy transfer is required, and one can use the K–H–M equation to probe into this matter. The K–H–M equation in its present form is not applicable to flows with variable densities (VDs), and a further generalisation to include VD effects is needed.

To understand the physical mechanisms that create negative production in t.k.e., we extend the K–H–M equation to VD flows and apply it to the Charonko & Prestridge (2017) experiments. In that work, one-point statistical energy budgets of the velocity fluctuations were analysed in detail using simultaneous measurements of both the velocity and the density fields. Variable-density effects were observed to be strong and led to significant differences in the advection, production, transport and dissipation of turbulent kinetic energy, $k = \overline{u_i^2}/2$. The most pronounced difference occurred at the jet centreline where the t.k.e. production term was negative. Here, we will use the extended K–H–M equation to help to explain these observations. A related use of the two-point statistical formulation of the K–H–M equation is reported in a series of papers by Danaila and coworkers (see Voivenel *et al.* (2016) and references therein). The group has studied the mixing of turbulent jets with variable viscosities while keeping the fluid density a constant. In Voivenel *et al.* (2016), a variable viscosity (VV) K–H–M equation was derived and the authors demonstrated an interesting feature of VV flows: the spatial gradients of viscosity are sources of t.k.e.

This paper contains a self-contained derivation of the VD K–H–M equation given in appendix A, and VD effects appear as extra terms in the equation. The constant-density version of the K–H–M equation is recalled briefly in § 2, which is followed by an explanation of the rationale behind the proposed generalisation to VD flows. Section 3 gives the details of the experimental dataset used for analysis. The approximations used to compute various terms in the new K–H–M equation are described. Section 4 describes the scale-by-scale energy transfer and § 5 the energy budget, with conclusions regarding these observations in § 6.

2. The K–H–M equation – the evolution of the second-order velocity structure function

The K–H–M equation is the evolution equation of the ensemble-averaged $\overline{(\cdot)}$ scale energy defined by $\overline{\delta q^2} = \overline{(\delta u_i)^2} = \overline{[u_i(\boldsymbol{x}) - u_i(\boldsymbol{x}')]^2}$, where $\boldsymbol{x}$ and $\boldsymbol{x}'$ are two points in physical space. Its derivation follows from a standard manipulation of the Navier–Stokes equations written down separately for the two points which can be found in, e.g., Gomes-Fernandes *et al.* (2015) and is therefore not repeated here. The full expression in Cartesian coordinates is given in the following equation and its components are labelled using the terminology in Valente & Vassilicos (2014):

$$\overbrace{\frac{\partial \overline{\delta q^2}}{\partial t} + \left(\frac{U_k + U_k'}{2}\right)\frac{\partial \overline{\delta q^2}}{\partial X_k}}^{\text{Advection } A} + \overbrace{\frac{\partial \overline{\delta u_k \delta q^2}}{\partial r_k}}^{\text{Nonlinear transport } \Pi} + \overbrace{\frac{\partial \delta U_k \overline{\delta q^2}}{\partial r_k}}^{\text{Linear transport } \Pi_U}$$
$$= \overbrace{-2\overline{\delta u_i \delta u_k}\frac{\partial \delta U_i}{\partial r_k} - \overline{(u_k + u_k')\delta u_i}\frac{\partial \delta U_i}{\partial X_k}}^{\text{Production } P}$$

https://doi.org/10.1017/jfm.2018.125 Published online by Cambridge University Press

$$-\overbrace{\frac{\partial}{\partial X_k}\left(\frac{\overline{(u_k+u_k')\delta q^2}}{2}\right)}^{\text{Turbulent transport } T}-\overbrace{\frac{2}{\rho}\frac{\partial\overline{\delta u_k \delta p}}{\partial X_k}}^{\text{Pressure transport } T_p}$$
$$+\overbrace{2\nu\frac{\partial^2\overline{\delta q^2}}{\partial r_k^2}}^{\text{Viscous diffusion } D_\nu}+\overbrace{\frac{\nu}{2}\frac{\partial^2\overline{\delta q^2}}{\partial X_k^2}}^{\text{Viscous diffusion } D_{\boldsymbol{X},\nu}}\overbrace{-2\nu\left[\overline{\left(\frac{\partial u_i}{\partial x_k}\right)^2}+\overline{\left(\frac{\partial u_i'}{\partial x_k'}\right)^2}\right]}^{\text{Dissipation } 4\bar{\epsilon}}, \tag{2.1}$$

where $\delta U_i = U_i - U_i'$, $\delta u_i = u_i - u_i'$ and $\delta p = p - p'$; U refers to the Reynolds-averaged mean velocity and u is the fluctuation. Unprimed variables are measured at the point $\boldsymbol{x}$ and primed variables are at $\boldsymbol{x}'$. The two spatial points are separated by a vector $\boldsymbol{r}$, $\boldsymbol{r} = \boldsymbol{x} - \boldsymbol{x}'$, and their centroid is $\boldsymbol{X} = (\boldsymbol{x} + \boldsymbol{x}')/2$. Equation (2.1) is a function of both scale and physical space, $\boldsymbol{r}$ and $\boldsymbol{X}$, of which the latter is responsible for transport and production of scale energy in spatially developing flows. In homogeneous isotropic flows, the scale energy $\overline{\delta q^2}$ is related to the one-dimensional energy spectrum $E(k)$ by the following equation (Davidson 2015, p. 90):

$$\overline{\delta q^2} \approx \int_{\pi/r}^{\infty} E(k)\,\mathrm{d}k + \frac{r^2}{\pi^2}\int_0^{\pi/r} k^2 E(k)\,\mathrm{d}k. \tag{2.2}$$

The first term on the right-hand side represents the sum of the kinetic energy of all scales smaller than r and the second term represents the contribution from the enstrophy $|\boldsymbol{\omega}|^2$ where $\boldsymbol{\omega}$ is a vector. For $r \gg \eta$, the Kolmogorov scale, the enstrophy contribution is negligible relative to the kinetic energy. The scale energy is therefore $\overline{\delta q^2} \approx \int_{\pi/r}^{\infty} E(k)\,\mathrm{d}k$. Using the established power law $E(k) \sim k^{-5/3}$, valid for scales inside the inertial subrange, the ratio of energies between scales that are a factor of two apart, e.g. r and $r/2$, is around 3.2. This means that $\overline{\delta q^2}$ is mainly the sum of energies of the first few scales (eddies) smaller than r. The kinetic energy of scale r contributes approximately 70 % to the sum, and $\overline{\delta q^2}$ can therefore be considered as representative of the energy at r. This interpretation breaks down near η, where the enstrophy contribution overwhelms the kinetic energy contribution, and this should be kept in mind when analysing the dissipative scales. Extension of (2.2) to general flows is straightforward and requires the three-dimensional energy spectrum, but the scale arguments made above still hold.

Some of the terms appearing in (2.1) are analogous to the advection A, production P, turbulent/pressure transport T/T_p, viscous diffusion D and dissipation $\bar{\epsilon}$ terms in the t.k.e. equation, hence their adopted notations. The interscale energy flux terms Π_U and Π are new and they represent the scale-by-scale linear and nonlinear energy flux in $\boldsymbol{r}$-space. Figure 1 shows a mechanistic picture of the roles of Π_U and Π in the energy transfer process among different turbulent eddy size classes in three-dimensional turbulent flows. Turbulent kinetic energy is injected into the fluid by forcing at scales of the order of the integral length scale L. This energy is passed down from large to small eddies until it is dissipated into heat by fluid viscosity at scales of the order of the Kolmogorov length scale η. Successive eddy size classes differing by a factor of two from $L/2$ to $L/32$ are represented by boxes of different sizes, and the number density of each class is represented by the number of eddies drawn inside the box. The role of Π is to transfer scale energy from one size class to immediate neighbours. This local nature of energy transfer in the scale space is a

https://doi.org/10.1017/jfm.2018.125 Published online by Cambridge University Press

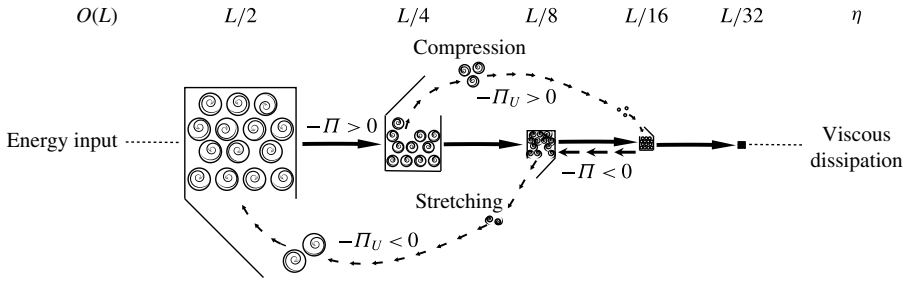


FIGURE 1. A cartoon illustrating the nature of the linear and nonlinear interscale transfer terms, Π_U and Π. Turbulent kinetic energy in the fluid is created by forcing mechanisms at scales of the order of the integral length scale L. This energy is then passed from large to small eddies until it gets converted (dissipated) into internal energy by fluid viscosity at scales of the order of the Kolmogorov length scale η. Each box in the figure represents one particular eddy size class, starting from $L/2$ down to $L/32$. The number density of each size class is represented by the number of eddies inside each box. Here, Π is a local process by which scale energy is transferred by turbulent velocity fluctuations between adjacent boxes with their number densities remaining constant during the process; Π_U, on the contrary, is the distortion of turbulent eddies due to the presence of mean flow gradients δU and in principle can be a non-local process by which scale energy is removed from a particular eddy size class and added to another one that need not be adjacent.

fundamental postulate in the Richardson–Kolmogorov phenomenology and has found substantial support in the very recent DNS study of three-dimensional homogeneous turbulence ($Re_\lambda = 315$ and Π_U is identically zero) reported by Cardesa, Vela-Martin & Jimenez (2017). These authors tracked the birth and death of eddies and showed that eddies of a given scale originate from eddies twice their scale, whereas they give rise to eddies half their scale before disappearing. In contrast, Π_U represents the energy loss/gain at a particular eddy size class due to the distortion of the eddy, including changes in size and orientation, by mean flow gradient δU; this can be seen by writing $\Pi_U = (\partial \delta U_k \overline{\delta q^2})/\partial r_k = \overline{\delta q^2}(\partial \delta U_k/\partial r_k) + \delta U_k(\partial \overline{\delta q^2}/\partial r_k)$. This process is represented in figure 1 by the removal of eddies (circles in a box) from the size class $L/4$ to the size class $L/16$; the eddies are compressed by δU. Because δU is flow-dependent, Π_U is, in principle, a non-local process and is therefore very different in nature from Π. In this sense, Π_U is not an energy cascade postulated in the Richardson–Kolmogorov phenomenology. To distinguish this significant difference between Π_U and Π, we will use 'transfer' to refer to the energy loss/gain at a particular scale by the linear term Π_U, and 'energy cascade' is reserved for the nonlinear term Π throughout this paper.

Under the assumptions of local equilibrium and homogeneity for scales in the inertial subrange, (2.1) simplifies to the following:

$$\frac{\partial \overline{\delta u_k \delta q^2}}{\partial r_k} \approx -2\nu \left[\overline{\left(\frac{\partial u_i}{\partial x_k} \right)^2} + \overline{\left(\frac{\partial u_i'}{\partial x_k'} \right)^2} \right] = -4\overline{\epsilon}. \tag{2.3}$$

This describes the nonlinear energy transfer of fluctuating energy from spherical shells centred at $\boldsymbol{X}$ with radius r to either spherical shells centred at the same $\boldsymbol{X}$ but

https://doi.org/10.1017/jfm.2018.125 Published online by Cambridge University Press

with different radius or within the same spherical shell but to a different orientation $\boldsymbol{r}/r$ (Valente & Vassilicos 2015). Equation (2.3) is a first-order partial differential equation with a non-homogeneous source term on the right. This means that once the dissipation is specified in the interior and on the boundaries of the domain ($\boldsymbol{r}$-space), the equation evolves accordingly and the dynamics is independent of the geometry, inhomogeneity and anisotropy of the large scales insofar as they only set the dissipation rate (Davidson 2015). This is the crux of Richardson–Kolmogorov cascade and is postulated to be universal for any flow. It can be further simplified by assuming local isotropy and by integration over a sphere of radius r, resulting in $\overline{\delta \boldsymbol{u}_{||}\delta q^2} \approx -(4/3)\overline{\epsilon} r$, and from which the 4/5-law for the longitudinal velocity third-order structure function can be derived, e.g. Monin & Yaglom (1975) and Rasmussen (1999).

The spatial flux term $T = -(\partial/\partial X_k)(\overline{(u_k + u_k')\delta q^2}/2)$ of (2.1) represents the transfer of scale energy in the physical space $\boldsymbol{X}$ by the fluctuating velocities. It serves to supply scale energy to regions where the production of energy is low, effectively sustaining turbulence in those regions. Examples are the bulk region near the centreline of a channel (Marati *et al.* 2004) or the edges of a turbulent jet (Charonko & Prestridge 2017).

2.1. *An alternative form of (2.1) with local isotropy*

An alternative form of the general K–H–M equation, (2.1), is obtained when one carries out an integration over a sphere of radius $r = |\boldsymbol{r}|$ and assumes local isotropy. For illustration purposes, we consider the simplified equation (2.3) for homogeneous and locally isotropic flows (see also Gomes-Fernandes *et al.* 2015), and this gives

$$-\overline{\delta u_1 \delta q^2} + 2\nu \frac{\mathrm{d}\overline{\delta q^2}}{\mathrm{d}r} = \frac{4}{3}\overline{\epsilon} r, \tag{2.4}$$

where δu_1 is the streamwise velocity increment and the second term is the integrated form of D_ν, which is the viscous contribution to the balance. This equation is valid across both inertial and dissipative subranges under the tenets of Kolmogorov's 1941 (K41) theory. An obvious limitation is clearly the restriction of isotropy, which is relevant to laboratory flows having small to moderate Taylor–Reynolds number ($<$1000, Shen & Warhaft (2000)). Moreover, in situations where K41 does not apply, it hides the directional dependence of the interscale energy flux, in which localised regions in the $\boldsymbol{r}$-space exhibiting an inverse energy cascade cannot be seen (see figures 16 and 17 in Gomes-Fernandes *et al.* (2015)). Nonetheless, this form has a clear advantage in experimental measurements performed with hot-wire anemometry in that structure functions need only be measured along the streamwise direction instead of over a volume. Extensions of the equation to include large-scale inhomogeneities that bring decay, production and transport to the scale energy have been made in jets by Burattini, Antonia & Danaila (2005), wakes by Thiesset *et al.* (2013) and grid turbulence by Danaila *et al.* (2004), to name a few. Very recently, Sadeghi published two papers (Sadeghi, Lavoie & Pollard 2015, 2016) on equilibrium similarity solutions of the scale energy equation of constant-density turbulent round jets. Because the present analysis utilises the full K–H–M equation, scale-by-scale energy budgets derived in previous works can differ from the present analysis at the large scales. The discrepancies, however, are deemed to be small in the inertial and dissipative range where the assumption of local isotropy holds approximately.

https://doi.org/10.1017/jfm.2018.125 Published online by Cambridge University Press

2.2. *Extension to VD flows*

When writing statistical equations for VD flows, the representation of correlations involving density fluctuations is not unique (Chassaing *et al.* 2002). We adopt the Favre-averaged (mass-weighted) formalism because the resulting equations resemble their constant-density counterparts; the Favre decomposition of an instantaneous variable mirrors the Reynolds decomposition. This allows one to recognise the original K–H–M equation in the new VD equation when density is a constant. As detailed in appendix A, a new notation is used for VD flows which is different from the notation in (2.1). Using Favre-averaging, the instantaneous velocities at two separate spatial points $\boldsymbol{x}$ and $\boldsymbol{x}'$ can be written as $u_i(\boldsymbol{x}) = \underline{U_i} + \underline{u_i'} = \underline{\tilde{U}_i} + \underline{u_i''}$ and $u_i(\boldsymbol{x}') = \underline{\underline{U_i}} + \underline{\underline{u_i'}} = \underline{\underline{\tilde{U}_i}} + \underline{\underline{u_i''}}$. A tilde denotes a Favre-averaged quantity, $\tilde{\phi} = \overline{\rho\phi}/\overline{\rho}$, and ϕ'' is the remaining Favrian fluctuation. Similarly, the densities at the two points are written as $\rho(\boldsymbol{x}) = \underline{\rho}$ and $\rho(\boldsymbol{x}') = \underline{\underline{\rho}}$.

The first step is to express the scale energy with a VD formulation. A naive extension of the scale energy $\overline{\delta q^2} = \overline{(\delta u_i)^2}$ (old notation) to VD flows would be $\overline{(\delta\rho u_i'')^2} = \overline{(\underline{\rho}\,\underline{u_i''} - \underline{\underline{\rho}}\,\underline{\underline{u_i''}})^2}$. However, this brings density-squared terms that have no obvious physical interpretations. Instead, we consider a VD analogue of $\overline{(\delta u_i')^2} = \overline{\underline{u_i'^2}} + \overline{\underline{\underline{u_i'^2}}} - 2\overline{\underline{u_i'}\,\underline{\underline{u_i'}}}$ (new notation) that shows that the scale energy in constant-density flows is related to the Reynolds stresses at the two points and the two-point Reynolds stress correlation. The VD analogue should reduce to $\overline{(\delta u_i')^2}$ when ρ is constant, and a possible candidate is given as follows:

$$\overline{\underline{\rho u_i''^2}} + \overline{\underline{\underline{\rho u_i''^2}}} - 2\left(\tfrac{1}{2}\overline{[\underline{\rho} + \underline{\underline{\rho}}]\underline{u_i''}\,\underline{\underline{u_i''}}}\right), \tag{2.5}$$

where $\overline{\underline{\rho u_i''}\,\underline{\underline{u_j''}}}$ is the single-point stress tensor in VD flows at $\boldsymbol{x}$. The last term, $(1/2)\overline{[\underline{\rho} + \underline{\underline{\rho}}]\underline{u_i''}\,\underline{\underline{u_i''}}}$, is the two-point stress tensor defined in Clark & Spitz (2005) and Clark (2015). A simple algebraic manipulation shows that this form reduces to $\overline{(\delta u_i')^2}$ by setting $\rho =$ constant and by recalling that the Favre fluctuation is equal to the Reynolds fluctuation ($u_i'' = u_i'$) when $\rho =$ constant. The above expression can be rewritten in a form similar to $\overline{(\delta u_i')^2}$,

$$\overline{(\delta u_i'')^2_\rho} = \overline{(\underline{u_i''} - \underline{\underline{u_i''}})(\underline{\rho u_i''} - \underline{\rho u_i''})} = \overline{\delta(u_i'')\delta(\rho u_i'')}. \tag{2.6}$$

This is the correct definition of the scale energy in VD flows whose transport equation can be derived from those of the single- and two-point stress tensors. As derived in appendix A, the full equation is

$$\begin{aligned}
&\frac{\partial\overline{(\delta u_i'')^2_\rho}}{\partial t} + \overbrace{\frac{(\tilde{\underline{U}}_k + \tilde{\underline{\underline{U}}}_k)}{2}\frac{\partial\overline{(\delta u_i'')^2_\rho}}{\partial X_k}}^{\text{Advection},A} + \overbrace{\frac{\partial\overline{\delta u_k''(\delta u_i'')^2_\rho}}{\partial r_k}}^{\text{Nonlinear transport},\Pi} + \overbrace{\frac{\partial\overline{\delta\tilde{U}_k(\delta u_i'')^2_\rho}}{\partial r_k}}^{\text{Linear transport},\Pi_U} \\
&\quad = \overbrace{-2[A_{ik} + B_{ik}]\frac{\partial\delta\tilde{U}_i}{\partial r_k} - [A_{ik} - B_{ik}]\frac{\partial\delta\tilde{U}_i}{\partial X_k}}^{\text{Production},P} - \overbrace{\frac{1}{2}\frac{\partial\overline{(\underline{u_k''} + \underline{\underline{u_k''}})(\delta u_i'')^2_\rho}}{\partial X_k}}^{\text{Turbulent transport},T} \\
&\quad\quad - \overbrace{\left\{\overline{[1 + \underline{\rho}/\underline{\underline{\rho}}]\frac{\partial(\underline{p'} - \underline{\underline{p'}})}{\partial\underline{\underline{x_i}}} + 2\frac{\partial(\underline{p'} - \underline{\underline{p'}})}{\partial\underline{x_i}}}\right\}\underline{u_i''} + \left\{\overline{[1 + \underline{\underline{\rho}}/\underline{\rho}]\frac{\partial(\underline{p'} - \underline{\underline{p'}})}{\partial\underline{x_i}} + 2\frac{\partial(\underline{p'} - \underline{\underline{p'}})}{\partial\underline{\underline{x_i}}}}\right\}\underline{\underline{u_i''}}}^{\text{Pressure transport},T_p}
\end{aligned}$$

https://doi.org/10.1017/jfm.2018.125 Published online by Cambridge University Press

Term	Description	Equation
$\overline{(\delta u_i'')^2_\rho}$	Scale energy in VD flows	(2.6)
A_{ik}, B_{ik}	Tensors appearing in scale-energy production term	(A 7)
$(\delta u_i)_a$, $(\delta u_i)_b$	Tensors appearing in scale-energy viscous term	(A 10)
τ_{ik}	Linear constitutive relation for Newtonian fluids	$\mu\left(\dfrac{\partial u_i}{\partial x_k}+\dfrac{\partial u_k}{\partial x_i}\right)$
a_i	One-point mass flux	$\overline{\rho u_i'}/\overline{\rho}$
$a_i(\boldsymbol{x},\boldsymbol{x}')$	Two-point mass flux	A(iii)
$T_{ii}(\boldsymbol{x},\boldsymbol{x}')$, $T_{ii}(\boldsymbol{x}',\boldsymbol{x})$	'Favre-avg. two-point stress–compressibility correlation'[a]	A(i)
$Q_i(\boldsymbol{x},\boldsymbol{x}')$, $Q_i(\boldsymbol{x}',\boldsymbol{x})$	'Favre-avg. two-point fluctuating momentum'	A(ii)
$\underline{\underline{R_{ik}}}$, $\underline{\underline{R_{ik}}}$	Favre-avg. one-point stress	$\overline{\underline{\underline{\rho u_i'' u_k''}}}$, $\overline{\underline{\underline{\rho u_i'' u_k''}}}$

TABLE 1. Descriptions of terms appearing in the VD K–H–M equation (2.7). The fluid is assumed to be incompressible.

[a]Different from the two-point stress tensor $R_{ii}(\boldsymbol{x},\boldsymbol{x}')=(\overline{[\underline{\rho}+\underline{\underline{\rho}}]\underline{u_i''}\,\underline{\underline{u_i''}}})/2$ (Clark 2015).

$$
\begin{aligned}
&\overbrace{+\,2\mu\left\{\overline{\frac{\partial}{\partial \underline{x}_k}\left[(\delta u_i')\frac{\partial(\underline{u_i'}-\underline{\underline{u_i'}})}{\partial \underline{x}_k}\right]+\frac{\partial}{\partial \underline{\underline{x}}_k}\left[(\delta u_i')\frac{\partial(\underline{u_i'}-\underline{\underline{u_i'}})}{\partial \underline{\underline{x}}_k}\right]}\right\}}^{\text{Viscous diffusion},D_\nu+D_{\boldsymbol{X},\nu}}\\
&\overbrace{-\,2\mu\left\{\overline{\left(\frac{\partial \underline{u_i'}}{\partial \underline{x}_k}\right)\left(\frac{\partial \underline{u_i'}}{\partial \underline{x}_k}\right)}+\overline{\left(\frac{\partial \underline{\underline{u_i'}}}{\partial \underline{\underline{x}}_k}\right)\left(\frac{\partial \underline{\underline{u_i'}}}{\partial \underline{\underline{x}}_k}\right)}\right\}}^{\text{Dissipation},4\overline{\epsilon}}+\underbrace{\overline{\frac{\Delta\rho}{\underline{\rho}}\underline{u_i''}\frac{\partial \underline{\tau_{ik}'}}{\partial \underline{x}_k}}-\overline{\frac{\Delta\rho}{\underline{\underline{\rho}}}\underline{\underline{u_i''}}\frac{\partial \underline{\underline{\tau_{ik}'}}}{\partial \underline{\underline{x}}_k}}}_{\text{VD effects},\mu\Delta\rho}\\
&\underbrace{+\,2\{\underline{a_i}-a_i(\boldsymbol{x}',\boldsymbol{x})\}\frac{\partial \overline{P}}{\partial \underline{x}_i}+2\{\underline{\underline{a_i}}-a_i(\boldsymbol{x},\boldsymbol{x}')\}\frac{\partial \overline{\underline{\underline{P}}}}{\partial \underline{\underline{x}}_i}}_{\text{Mass-flux–pressure},a_P}\\
&\underbrace{-\,2\{\underline{a_i}-a_i(\boldsymbol{x}',\boldsymbol{x})\}\frac{\partial \overline{\tau_{ik}}}{\partial \underline{x}_k}-2\{\underline{\underline{a_i}}-a_i(\boldsymbol{x},\boldsymbol{x}')\}\frac{\partial \overline{\underline{\underline{\tau_{ik}}}}}{\partial \underline{\underline{x}}_k}}_{\text{Mass-flux–stress},a_\tau}\\
&\underbrace{-\,\{T_{ii}(\boldsymbol{x},\boldsymbol{x}')+T_{ii}(\boldsymbol{x}',\boldsymbol{x})\}}_{T_{VD}}\underbrace{-2\left\{\frac{Q_i(\boldsymbol{x},\boldsymbol{x}')}{\overline{\underline{\underline{\rho}}}}\frac{\partial \underline{\underline{R_{ik}}}}{\partial \underline{\underline{x}}_k}+\frac{Q_i(\boldsymbol{x}',\boldsymbol{x})}{\overline{\underline{\rho}}}\frac{\partial \underline{\underline{R_{ik}}}}{\partial \underline{x}_k}\right\}}_{Q}.
\end{aligned}
\tag{2.7}
$$

Table 1 provides a reference for the various terms appearing in (2.7), many of which are defined in appendix A. By setting $\tilde{U}_i=\overline{U_i}$ and $u_i''=u_i'$, the A, Π, Π_U, T and $4\overline{\epsilon}$ terms revert to their constant-density counterparts. With a little more algebra, the P, T_p, D_ν and $D_{\boldsymbol{X},\nu}$ terms will also behave similarly. The remaining five terms, $\mu\Delta\rho$, a_P, a_τ, T_{VD} and Q, arise due to VD effects. When $\rho=$ constant, they drop out from the equation and one recovers the original K–H–M equation.

https://doi.org/10.1017/jfm.2018.125 Published online by Cambridge University Press

2.3. *The Kolmogorov 4/5-law in VD flows*

In homogeneous and local-equilibrium flows, (2.7) admits the VD analogue of the constant-density Kolmogorov equation ((2.3), with the viscous diffusion term included),

$$\Pi = D_\nu + D_{\boldsymbol{X},\nu} - 4\overline{\epsilon} + (\mu\Delta\rho + a_P + a_\tau - T_{VD} - Q). \tag{2.8}$$

It contains the extra five terms due to VD effects. Because the $4\overline{\epsilon}$ term has the same form as its counterpart in constant-density flows (see (2.1)), $\overline{\epsilon}$ will have a constant prefactor of $4/5$ when an integration over a sphere of radius $r = |\boldsymbol{r}|$ under the assumption of local isotropy is first carried out on (2.8). After further algebraic manipulations using several vector identities derived from the Navier–Stokes equations, one obtains the $4/5$ prefactor. A detailed description of the procedures involved is given by Rasmussen (1999).

A further simplification results when $r \to 0$ (the same as $\boldsymbol{x} \to \boldsymbol{x}'$), i.e. scales within the viscous dissipation subrange. In this case, we have $\Delta\rho = \underline{\rho} - \underline{\underline{\rho}} \to 0$, $a_i(\boldsymbol{x}', \boldsymbol{x}) \to \underline{a_i}$ and $a_i(\boldsymbol{x}, \boldsymbol{x}') \to \underline{\underline{a_i}}$ and obtain the following equation:

$$0 = \overbrace{\mu\left\{\overline{\frac{\partial^2\delta q^2}{\partial x_k^2}} + \overline{\frac{\partial^2\delta q^2}{\partial \underline{\underline{x_k}}^2}}\right\}}^{D_\nu + D_{\boldsymbol{X},\nu}} - \overbrace{2\mu\left\{\overline{\left(\frac{\partial u_i'}{\partial \underline{x_k}}\right)\left(\frac{\partial u_i'}{\partial \underline{x_k}}\right)} + \overline{\left(\frac{\partial u_i'}{\partial \underline{\underline{x_k}}}\right)\left(\frac{\partial u_i'}{\partial \underline{\underline{x_k}}}\right)}\right\}}^{4\overline{\epsilon}} - \underbrace{\{T_{ii}(\boldsymbol{x}, \boldsymbol{x}') + T_{ii}(\boldsymbol{x}', \boldsymbol{x})\}}_{T_{VD}}. \tag{2.9}$$

This equation shows that the viscous dissipation of scale energy, t.k.e., in VD flows is modulated by the T_{VD} term which involves the instantaneous velocity divergence. In flows where sharp discontinuities in velocity and density are absent, the T_{VD} term is close to zero because of a divergence-free instantaneous velocity field. This means that in the viscous dissipation subrange, the final dissipation of kinetic energy in VD flows is the same as in constant-density flows with $D_\nu = 4\overline{\epsilon}$, where the diffusion of scale energy in physical space $D_{\boldsymbol{X},\nu}$ is negligible (Valente & Vassilicos 2014).

3. Variable-density jet experiments

The experimental dataset to be analysed was recently reported in Charonko & Prestridge (2017). Key characteristics of this dataset are provided below and readers are referred to Charonko & Prestridge (2017) for more details. A gas jet, a mixture of either air + acetone or SF_6+ acetone, was injected vertically downward from a nozzle into a coflow set up inside a wind tunnel. The two jets were matched by their bulk Reynolds number (∼20 000). For the air jet, the density ratio was 1.2, and that of the SF_6 jet was 4.2. Simultaneous planar laser-induced fluorescence (PLIF) and two-dimensional two-component particle image velocimetry (2D2C-PIV) measurements were carried out for both jets at three downstream locations, $2d$, $16d$ and $30d$, where $d = 11$ mm is the nozzle diameter. A definition diagram of the experimental set-up is shown in figure 2 with representative measurement field locations. The computed two-dimensional vector fields are uniformly spaced at 0.287 mm in both directions. Table 2 tabulates the measurement resolution and parameters of the jets at each station.

https://doi.org/10.1017/jfm.2018.125 Published online by Cambridge University Press

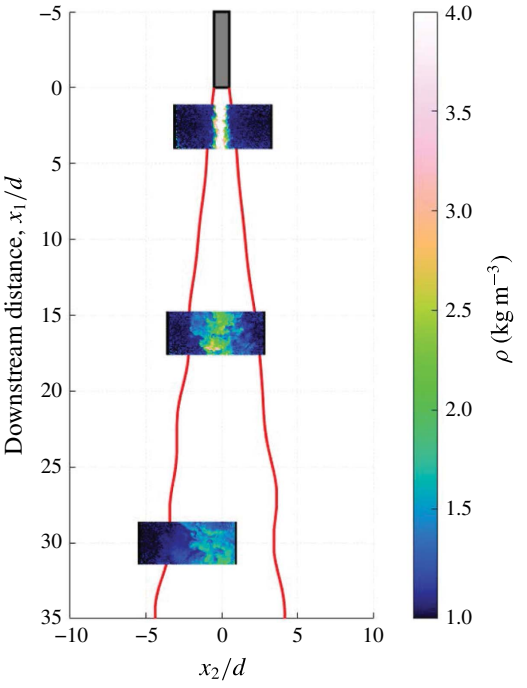


FIGURE 2. A schematic diagram of the VD turbulent round jet experiments in Charonko & Prestridge (2017). Jet diameter $d = 11$ mm.

Station	Exp. resolution	$b_{1/2}$ (mm)	L_{11}/L_{22} (mm)	η (mm)	λ (mm)	Re_λ
Air jet						
$x_1 = 16d$	$7.0\eta \times 7.0\eta$	11.3	4.77/4.43	0.041	1.216	216
$x_1 = 30d$	$4.4\eta \times 4.4\eta$	21.8	6.60/6.92	0.066	1.725	168
SF_6 jet						
$x_1 = 16d$	$5.8\eta \times 5.8\eta$	9.6	4.22/3.79	0.050	1.135	131
$x_1 = 30d$	$3.6\eta \times 3.6\eta$	17.5	6.06/5.94	0.081	1.753	92

TABLE 2. Experimental conditions. Kolmogorov length scale $\eta = (\nu^3/\overline{\epsilon})^{1/4}$, Taylor microscale $\lambda = \sqrt{15\nu\overline{u_1'^2}/\overline{\epsilon}}$, $\overline{\epsilon}$ = mean dissipation rate and Taylor Reynolds number $Re_\lambda = \sqrt{\overline{u_1'^2}}\lambda/\nu$. The dynamic kinematic viscosity μ is 1.7×10^{-5} kg m^{-1} s^{-1} for the air jet and 1.55×10^{-5} kg m^{-1} s^{-1} for the SF_6 jet. Because the flow is inhomogeneous, $\overline{\epsilon}$ is computed as $\overline{\epsilon}_\rho/\overline{\rho}_c$, where $\overline{\rho}_c \equiv$ local centreline density and $\overline{\epsilon}_\rho = 2\mu\{\overline{(\partial u_i'/\partial x_k)(\partial u_i'/\partial x_k)} + \overline{(\partial u_i'/\partial x_k)(\partial u_i'/\partial x_k)}\}$ (see also § 3.3). Similarly, ν is computed by $\mu/\overline{\rho}_c$. Here, L_{11} and L_{22} represent the Eulerian integral length scale in the (x_1) streamwise and (x_2) radial directions; $b_{1/2}$ is the jet velocity half-width, defined as the radial position where the Favre-averaged streamwise velocity $\tilde{U}_1$ is one-half of the jet centreline value.

3.1. *Statistical convergence*

The acquisition frequency of the combined PIV/PLIF measurements was 1 Hz, and 10 000 snapshots were taken at each downstream location. Because the longitudinal

https://doi.org/10.1017/jfm.2018.125 Published online by Cambridge University Press

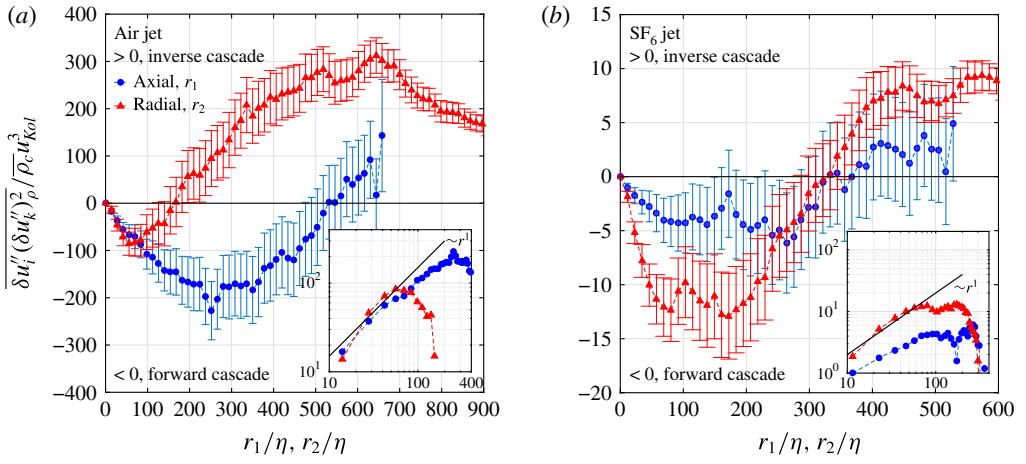


FIGURE 3. The third-order velocity structure function $\overline{\delta u_i''(\delta u_k'')_\rho^2}$ (nonlinear interscale transfer term Π) normalised by $\overline{\rho_c}$ and the Kolmogorov velocity scale $u_{Kol} = \sqrt[4]{\nu\epsilon}$ at $x_1 = 16d$ in (*a*) the air jet and (*b*) the SF$_6$ jet. The error bar shown indicates a 95 % confidence interval of $\overline{\delta u_i''(\delta u_k'')_\rho^2}$. The insets show $-\overline{\delta u_i''(\delta u_k'')_\rho^2}/\overline{\rho_c}u_{Kol}^3$ in a log–log plot and highlight the r^1 dependence for scales in the inertial subrange.

(downstream) Eulerian integral time scale is of the order of 0.1 s, the data ensemble can be considered as consisting of 10 000 statistically independent samples. Figure 3 shows the third-order structure function $\overline{\delta u_i''(\delta u_k'')_\rho^2}$ versus the separation distances r_1 and r_2, with error bars constructed from two standard deviations of each data point, giving a 95 % confidence interval for the mean. The standard deviation of $\overline{\delta u_i''(\delta u_k'')_\rho^2}$ is calculated from the square root of the variance of $\delta u_i''(\delta u_k'')_\rho^2$,

$$\mathrm{Var}(\overline{\delta u_i''(\delta u_k'')_\rho^2}) = \frac{1}{N}[\overline{(\delta u_i''(\delta u_k'')_\rho^2)^2} - \overline{\delta u_i''(\delta u_k'')_\rho^2}^2], \tag{3.1}$$

where $N = 10\,000$ is the number of independent samples. The third-order structure function converges to within ±30 %–40 % of the mean. In figure 3(*a*), the air jet structure function shows that when r/η is small, $\overline{\delta u_i''(\delta u_k'')_\rho^2}$ is negative, signifying a forward cascade (2.4). As r/η increases, the curves in both the axial (r_1) and radial (r_2) directions eventually become positive. The zero-crossing point, at larger scales in the axial direction, suggests that the forward cascade persists to larger scales along the jet axis. In the SF$_6$ jet, figure 3(*b*), the normalised magnitudes of the cascade in both directions are much smaller than those in the air jet and the zero-crossing points for the axial and radial directions are both at $r/\eta \approx 325$.

A physical interpretation is that heavy fluids in the SF$_6$ jet suppress the energy transfer among scales, and this is most severe along the jet centreline. There are two expected power laws on r, namely r^3 for $r \sim O(\eta)$ and r^1 for r within the inertial subrange. The former results from applying a Taylor series expansion to $\delta u_i = u_i - u_i' = -\nabla u_i \cdot \boldsymbol{r} \sim |\boldsymbol{r}|$ if the small scales are isotropic (this is satisfied to within 15 % in figure 5). Hence, $\overline{\delta u_i''(\delta u_k'')_\rho^2} \sim r^3$, where $r = |\boldsymbol{r}|$. The latter is a consequence of (2.4). Because the smallest resolved scale in the present study is approximately 10η, only the r^1 power law is captured (see insets).

https://doi.org/10.1017/jfm.2018.125 Published online by Cambridge University Press

3.2. *Degree of isotropy of fluctuations in velocity, vorticity and scale energy*

The ratios of the second moments of the velocity derivatives are used to test for local isotropy (Taylor 1935); these isotropic relations are

$$\frac{\left\langle \left(\dfrac{\partial u_1'}{\partial x_2}\right)^2 \right\rangle}{\left\langle \left(\dfrac{\partial u_1'}{\partial x_1}\right)^2 \right\rangle} = \frac{\left\langle \left(\dfrac{\partial u_2'}{\partial x_1}\right)^2 \right\rangle}{\left\langle \left(\dfrac{\partial u_1'}{\partial x_1}\right)^2 \right\rangle} = 2, \quad \frac{-\left\langle \dfrac{\partial u_1'}{\partial x_2}\dfrac{\partial u_2'}{\partial x_1} \right\rangle}{\left\langle \left(\dfrac{\partial u_1'}{\partial x_1}\right)^2 \right\rangle} = 0.5 \tag{3.2a,b}$$

and

$$\frac{\left\langle \left(\dfrac{\partial u_2'}{\partial x_2}\right)^2 \right\rangle}{\left\langle \left(\dfrac{\partial u_1'}{\partial x_1}\right)^2 \right\rangle} = 1, \quad \frac{\langle \omega_3^2 \rangle}{\left\langle \left(\dfrac{\partial u_1'}{\partial x_1}\right)^2 \right\rangle} = 5. \tag{3.3a,b}$$

Figure 4 shows how these ratios evolve along the centrelines of the two jets at two different downstream locations. The jets are not isotropic for $x_1/d \leqslant 30$, except for the radial moments in both jets, nor are the radial profiles for $|x_2/b_{1/2}| < 1.8$ (not shown). This is in congruence with experimental data by Ganapathisubramani, Lakshminarasimhan & Clemens (2007). The ratios also become slightly more isotropic at $x_1/d = 30$.

The variable density of the SF_6 jet does not appear to affect these ratios, which have values close to their counterparts in the air jet. The mean-square velocity gradients are representative of a range of scales since, for example, $\overline{(\partial u_1'/\partial x_1)^2} = \int_0^\infty k_1^2 E_{11}(k_1)\,\mathrm{d}k_1$, where $E_{11}(k_1)$ is the one-dimensional streamwise spectrum. To assess the level of isotropy at each r, the measured distribution of $\overline{(\delta u_2'')^2}_\rho$ is compared with that calculated with the following isotropic relation (Monin & Yaglom 1975; Lavoie, Djenidi & Antonia 2007):

$$\overline{(\delta u_2'')^2}_{\rho\,cal} = \frac{r}{2}\frac{\mathrm{d}\overline{(\delta u_1'')^2}_\rho}{\mathrm{d}r} + \overline{(\delta u_1'')^2}_\rho, \tag{3.4}$$

where the measured distribution of $\overline{(\delta u_1'')^2}_\rho$ is used as the input. The prediction is plotted as the ratio $\overline{(\delta u_2'')^2}_{\rho\,cal}/\overline{(\delta u_2'')^2}_\rho$ in figure 5. Figure 5 shows isotropy, satisfied to within 15 % for length scales $r/\lambda < 2$, in both the air and the SF_6 jet for the two downstream measurement locations. This is consistent with the structure function calculations of figure 3 because $\lambda \approx 30\eta$. As r grows, rapid departure from isotropy begins in the range $r/\lambda \in [3, 5]$, which is also where the streamwise Eulerian length scale L_{11} lies. At the largest separations, which are of the same size as $b_{1/2}$, the ratio is between 1.5 and 1.7. This is comparable to the one-point anisotropy ratio $\overline{u_1''^2}/\overline{u_2''^2}$ (Charonko & Prestridge 2017).

Isotropy improves with x_1/d for the air jet, while it is impaired by the VD effects in the SF_6 jet at the same streamwise location. This illustrates the usefulness of the two-point formulation since density effects cannot be unambiguously identified in the ratios of velocity-derivative moments (figure 4).

https://doi.org/10.1017/jfm.2018.125 Published online by Cambridge University Press

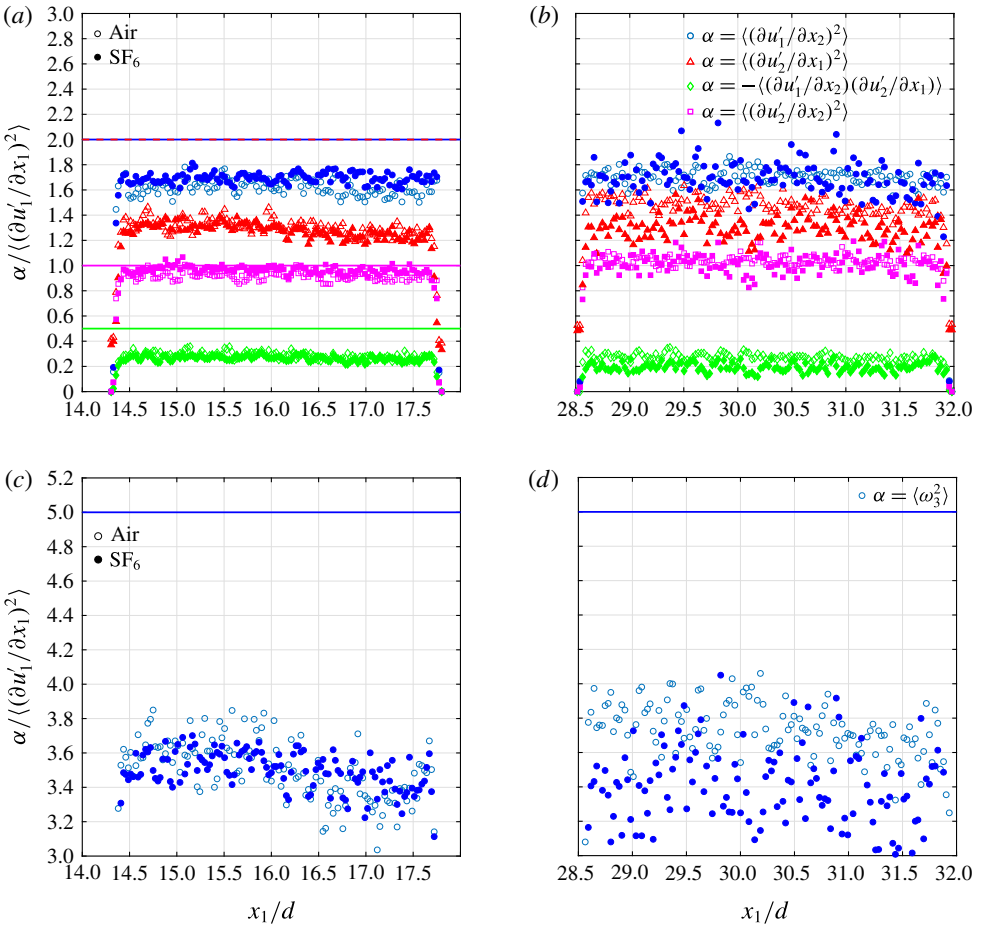


FIGURE 4. Streamwise evolution of the ratios of the second moments of the velocity derivatives measured at the jet centrelines for air and SF_6 at (*a*,*c*) $x_1/d = 16$ and (*b*,*d*) $x_1/d = 30$.

3.3. *Method of computation of terms in the VD K–H–M equation*

To understand scale energy transfer among spherical energy shells of different radii, we transform the experimental data from a Cartesian grid $(x_1, x_2, x_3) = (x_1, x_2, 0)$ to a spherical coordinate system (r, θ, ϕ). As the dataset is 2D, we effectively have a slice at $\phi = 0$ that is a polar grid (r, θ). We do not have the full range of all possible orientations of the vector $\boldsymbol{r}/r$, but this is not expected to cause serious issues in the interpretation of results because of jet axisymmetry. Bilinear interpolation is used during the coordinate transformation, in which (r, θ) are each partitioned into 80 equidistant points. A convergence study of the interpolation process showed that the transformation results were within $\pm 5\,\%$ as long as over 30 points were used, with larger numbers of points reducing the jitter in the interpolation. In the following, the computation of terms in (2.7) is described.

https://doi.org/10.1017/jfm.2018.125 Published online by Cambridge University Press

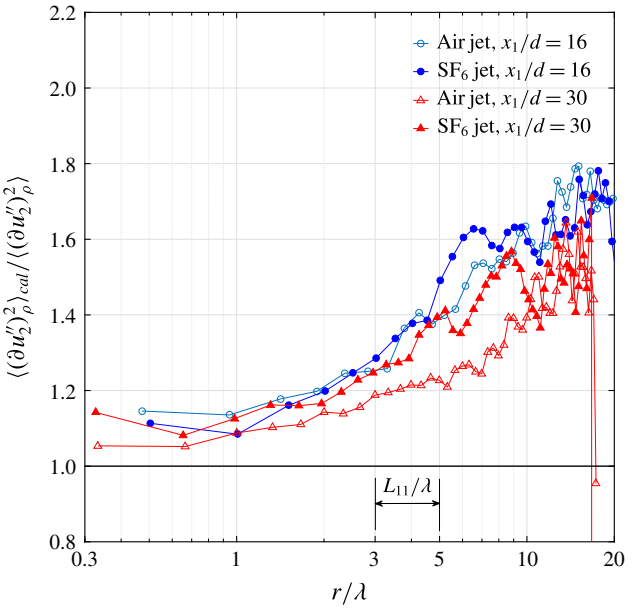


FIGURE 5. Ratio of $\overline{(\delta u_2'')^2}$ calculated using (3.4) to that from experimental data for the air jet (open symbols) and the SF_6 jet (filled symbols). The isotropic value of the ratio is one and L_{11} is the streamwise Eulerian length scale.

(i) $\overline{(\delta u_i'')^2_\rho} = \overline{\delta(u_i'')\delta(\rho u_i'')} \approx \overline{\delta(u_1'')\delta(\rho u_1'')} + 2\overline{\delta(u_2'')\delta(\rho u_2'')}$; the missing out-of-plane velocity structure function $\overline{\delta(u_3'')\delta(\rho u_3'')}$ is approximated by the in-plane radial structure function $\overline{\delta(u_2'')\delta(\rho u_2'')}$.

(ii) $\partial\overline{(\delta u_i'')^2_\rho}/\partial t = 0$ since the jet flow is stationary in the Eulerian frame.

(iii) $A = ((\underline{\tilde{U}_k} + \underline{\underline{\tilde{U}_k}})/2)(\partial\overline{(\delta u_i'')^2_\rho}/\partial X_k) \approx ((\underline{\tilde{U}_1} + \underline{\underline{\tilde{U}_1}})/2)(\partial\overline{(\delta u_i'')^2_\rho}/\partial X_1)$ since the mean flow is flowing predominantly downstream with $\tilde{U}_2 \approx \tilde{U}_3 \approx 0$, and, therefore, the advection in the radial r (x_2) and out-of-plane (x_3) directions is negligible in comparison. The streamwise gradient $\partial/\partial X_1$ is evaluated using a backward difference with spacing of 20 PIV vectors ($\approx$5.8 mm = 0.5–0.6$b_{1/2}$). The results are not sensitive to separations in the range of 10–20 vector spacings.

(iv) $\Pi = \partial\overline{\delta u_k''(\delta u_i'')^2_\rho}/\partial r_k \approx (1/r^2)(\partial(r^2\overline{\delta u_\parallel''(\delta u_i'')^2_\rho})/\partial r) + (1/r\sin\theta)\times(\partial\sin\theta\overline{\delta u_\perp''(\delta u_i'')^2_\rho}/\partial\theta)$, following the approach in Valente & Vassilicos (2015).

(v) $\Pi_U = \partial\delta\tilde{U}_k\overline{(\delta u_i'')^2_\rho}/\partial r_k$ is the linear energy flux across $\boldsymbol{r}$-space by the differential mean velocity $\delta\tilde{U}_k$, and is evaluated in the same way as Π.

(vi) $P = -2[A_{ik} + B_{ik}](\partial\delta\tilde{U}_i/\partial r_k) - [A_{ik} - B_{ik}](\partial\delta\tilde{U}_i/\partial X_k)$; the full expression is computed with the available 2D data.

(vii) $T \approx -(1/2)(\partial\overline{(\underline{u_1''} + \underline{\underline{u_1''}})(\delta u_i'')^2_\rho}/\partial X_1) - (1/2)(\partial\overline{(\underline{u_2''} + \underline{\underline{u_2''}})(\delta u_i'')^2_\rho}/\partial X_2)$; the streamwise gradient $\partial/\partial X_1$ is computed in the same manner as the advection term. The radial gradient $\partial/\partial X_2$, however, is computed using a spacing of 10 PIV vectors ($\approx$2.9 mm = 0.26–0.3$b_{1/2}$) radially from the jet centreline. A smaller spacing is used because of larger gradients in the radial than the streamwise direction.

https://doi.org/10.1017/jfm.2018.125 Published online by Cambridge University Press

(viii) T_p is estimated with Lumley's pressure transport model (Lumley (1979), see § 5.2).

(ix) $D_\nu \approx (2\nu/r^2)(\partial(r^2(\partial\overline{\delta q^2}/\partial r))/\partial r)$, following the approach in Valente & Vassilicos (2015). It represents viscous diffusion of energy $\overline{\delta q^2}$ across $\boldsymbol{r}$-space and is only significant for scales that are of the same order as η.

(x) $D_{X,\nu} = (\nu/2)(\partial^2\overline{\delta q^2}/\partial X_k^2)$ is the $\overline{\delta q^2}$ diffusion in physical centroidal space $\boldsymbol{X}$ and is essentially zero for the present jets, as shown in § 5.2. The second derivative is computed using the standard five-point stencil of the Laplacian.

(xi) $4\overline{\epsilon} = 2\mu\{\overline{(\partial\underline{u}_i'/\partial\underline{x}_k)(\partial\underline{u}_i'/\partial\underline{x}_k)} + \overline{(\partial\underline{\underline{u}}_i'/\partial\underline{\underline{x}}_k)\,(\partial\underline{\underline{u}}_i'/\partial\underline{\underline{x}}_k)}\}$ is directly calculated using the available 2D data with the expression in Tanaka & Eaton (2007).

(xii) $\mu\Delta\rho$ is computed from the available 2D data. This term scales as $1/Re$ (this follows from the momentum equations) because of $\partial\underline{\tau}_{ik}'/\partial\underline{x}_k$ and $\partial\underline{\underline{\tau}}_{ik}'/\partial\underline{\underline{x}}_k$ and is expected to be small. Its maximum magnitude occurs around λ and is less than 0.1 % of the dissipation rate $4\overline{\epsilon}$. It is therefore left out in the spherically averaged scale-by-scale energy budget to be discussed in § 5.2.

(xiii) a_P is computed with the measured mass flux and the inferred mean pressure gradients from the Favre-averaged mean momentum equations (Charonko & Prestridge 2017).

(xiv) a_τ is not computed as it is 3–4 orders of magnitude smaller than a_P (Charonko & Prestridge 2017).

(xv) T_{VD} and Q are computed directly from available 2D data.

Finally, all gradients in $\boldsymbol{r}$-space are computed with the standard second-order central difference. The evolution equation of $\overline{(\delta u_i'')_\rho^2}$ is a function of two spaces, $\boldsymbol{X}$ and $\boldsymbol{r}$. To calculate $\boldsymbol{X}$ derivatives, as needed in the advection term A, by using finite differencing on the discrete experimental data, one needs to evaluate $\overline{\delta q^2}$ at $\boldsymbol{X} + \mathrm{d}\boldsymbol{X}$ and subsequently form, for example, the difference $\overline{\delta q^2}(\boldsymbol{r}; \boldsymbol{X} + \mathrm{d}\boldsymbol{X}) - \overline{\delta q^2}(\boldsymbol{r}; \boldsymbol{X})$ for a forward-Euler approximation of the first derivative at $\boldsymbol{X}$. The overall physical interpretation of the equation should be recognised as the energy balance at a single point $\boldsymbol{X}$ under the interactions of a broad spectrum of eddy sizes $|\boldsymbol{r}|$ that are oriented in different directions $\boldsymbol{r}/|\boldsymbol{r}|$ relative to the origin $\boldsymbol{X}$. In practice, the term 'broad' is restricted by the spatial resolution of the experiment or of the numerical simulation. The smallest resolved scale of the jet experiments is approximately 34 %–48 % of the Taylor microscale.

In all subsequent plots, $(X_1, X_2) = (x_1, x_2) = (16d, 0)$, and this corresponds to the midheight of the field of view (FOV) of the combined PLIF/PIV experiments; this choice allowed us to calculate the largest possible range of streamwise separations r_1 from the data. The required two-point correlations are all symmetric differences with respect to this fixed (X_1, X_2).

3.4. *The appropriateness of the new definition of scale energy, $\overline{(\delta u_i'')_\rho^2}$, for VD flows*

The constant- and VD versions of the K–H–M equation both describe the evolution of scale energy. The new definition (2.6) of the scale energy incorporates density as a dynamically significant variable into the original formulation. Its effectiveness in VD flows is demonstrated below using the experimental data.

The VD and single-fluid definitions for scale energy, $\overline{(\delta u'')_\rho^2}$ and $\overline{\delta q^2}$, are shown in figure 6 for both jets at $x_1 = 16d$. The former is normalised by $\overline{\rho}\tilde{U}^2$ (the dimension of $\overline{(\delta u_i'')_\rho^2}$ is $([M]/[L^3])([L^2]/[T^2])$) and the latter by $\overline{U}^2$. The separation distances r_1

https://doi.org/10.1017/jfm.2018.125 Published online by Cambridge University Press

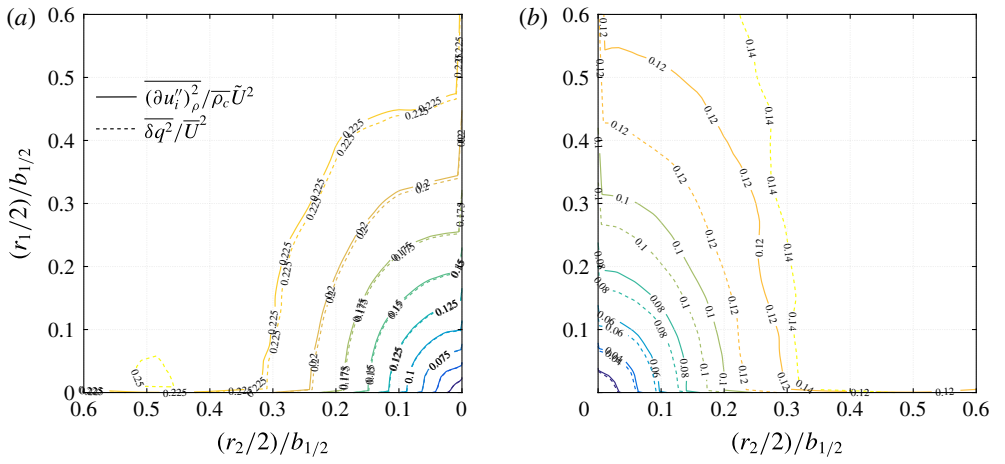


FIGURE 6. Comparison between the VD (2.6) and single-fluid definitions of scale energy, $\overline{(\delta u_i'')^2}_\rho/\overline{\rho_c}\tilde{U}^2$ (solid lines) and $\overline{\delta q^2}/\overline{U}^2$ (dotted lines). The experiments are at $x_1 = 16d$ for (*a*) the air jet and (*b*) the SF_6 jet. Here, r_1 and r_2 are the separation distances in the streamwise and radial directions.

and r_2 are normalised by the local velocity jet radius $b_{1/2}$. Several observations can be made. First, the two definitions yield essentially the same set of isocontours for the air jet, whereas they give drastically different results for the SF_6 jet. The equality of the two sets of contours gives $\overline{(\delta u_i'')^2}_\rho = \overline{\rho}\overline{\delta q^2}$ (note that $\tilde{U} \approx \overline{U} \gg$ mass flux $a_i = \overline{\rho u_i'}/\overline{\rho}$), meaning that the density is not dynamically relevant and can be treated as constant. The local Atwood number $At = (s-1)/(s+1)$ based on the centreline density, where s is the density ratio, is 0.043 for the air jet and 0.33 for the SF_6 jet. The air jet result is consistent with the commonly accepted upper limit ($= 0.05$) of At for Boussinesq flows (Livescu *et al.* 2010). On the other hand, the difference in the contours in the SF_6 jet reflects the non-Boussinesq character of the heavy jet and supports the use of $\overline{(\delta u'')^2}_\rho$ to capture VD effects.

Second, in the heavy jet, the agreement between the two sets of contours improves when r_1 and r_2 decrease. This indicates that the small scales are relatively immune to VD effects in the jet and provides empirical evidence supporting the discussions of (2.9). In the absence of strong density discontinuities, such as shock fronts, the dissipation mechanism of fluid energy in VD flows is akin to that in constant-density flows.

Third, regardless of their definitions, the tendency of small scales towards isotropy is evident because as r_1 and r_2 decrease, the contours progressively become more circular. However, as we have seen in figures 4 and 5, the approach to local isotropy is neither complete nor perfect. The above discussion demonstrates the appropriateness of our new definition of scale energy (2.6) in VD flows. In the ensuing sections, terms in the VD K–H–M equation (2.7) are analysed.

4. Scale-by-scale energy transfer

4.1. *Directionally dependent interscale transfer*

As discussed in § 2, the strength of the two-point K–H–M equation is the appearance of the interscale energy transfer terms, Π_U and Π, with their sum giving the total

https://doi.org/10.1017/jfm.2018.125 Published online by Cambridge University Press

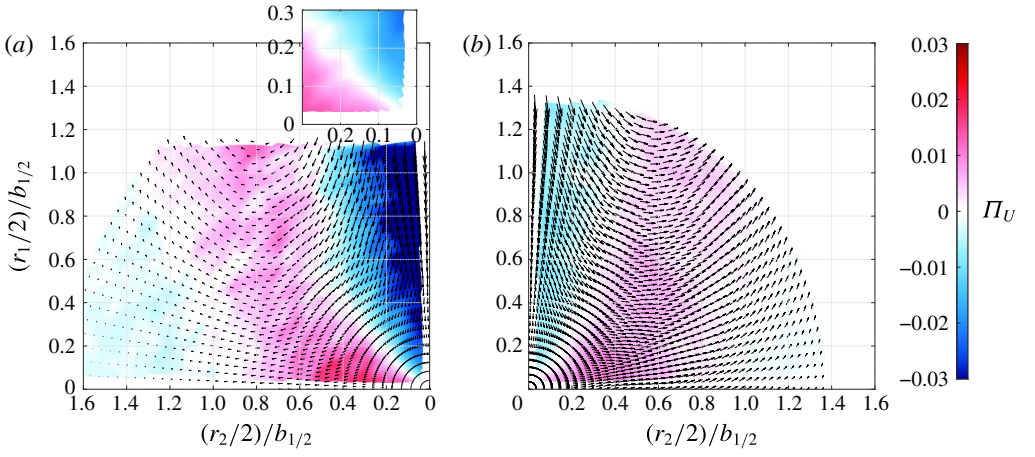


FIGURE 7. Linear interscale energy transfer $\Pi_U = (\partial \delta \tilde{U}_k \overline{(\delta u_i'')^2_\rho})/\partial r_k$ in (a) the air jet and (b) the SF_6 jet at $x_1 = 16d$. The vector field, $\delta \tilde{U}_k \overline{(\delta u_i'')^2_\rho}$, is overlaid on the Π_U colour map. The inset in (a) shows a close-up of Π_U of the air jet near the origin.

energy transfer rate across the scale r. Mathematically, these terms are the divergences of the vector fields, $\delta \tilde{U}_k \overline{(\delta u_i'')^2_\rho}$ and $\overline{\delta u_k'' (\delta u_i'')^2_\rho}$, in the $\boldsymbol{r}$-space. Since a negative/positive divergence indicates a converging/diverging vector field, the direction of energy flux is thus from large/small to small/large scales. First, we look at the linear term at $x_1 = 16d$ of both jets in figure 7; Π_U is normalised by the jet centreline variable $\overline{\rho_c}(\tilde{U_c}^3/b_{1/2})$. Regions of blue indicate $\Pi_U < 0$, a forward energy transfer, and regions of red indicate $\Pi_U > 0$, an inverse energy transfer, with the transition $\Pi_U \approx 0$ in white. The corresponding vector field of Π_U, $\delta \tilde{U}_k \overline{(\delta u_i'')^2_\rho}$, indicates a forward transfer when the vectors point towards the origin. The separation distances are divided by two and then normalised by $b_{1/2}$; the division by two reflects the symmetric difference with respect to the jet centreline from which terms like $\delta \tilde{U}_k$ are calculated.

The air jet interscale energy transfer shown in figure 7(a) shows a strong forward transfer in the jet axial direction, as indicated by the dark blue. The axial forward energy transfer in the air jet is over the entire range of scales measured and is a result of the decay of the mean centreline jet velocity.

The sign change of Π_U along approximately the 45° line for the air jet reflects the inhomogeneity of the flow due to a sign change in the mean entrainment (radial) velocity at that location (Lee & Chu 2003). In spatially homogeneous flows, e.g. grid turbulence (Gomes-Fernandes *et al.* 2015), there is no differential in the mean flow, so Π_U is zero.

The situation is slightly different for the heavy SF_6 jet in figure 7(b). A wide range of off-axis eddies exhibiting an inverse transfer (red region) penetrates down to the smallest resolved scales ($\approx 12\eta$) in the experiment. Signatures of the mean jet centreline and radial entrainment velocities, as discussed for the air jet, can still be seen in the axially and radially aligned eddies, but these are confined to a narrower region close to the centreline.

The term Π is the nonlinear mechanism responsible for the transfer of kinetic energy among turbulent length scales. The traditional energy cascade is nominally

https://doi.org/10.1017/jfm.2018.125 Published online by Cambridge University Press

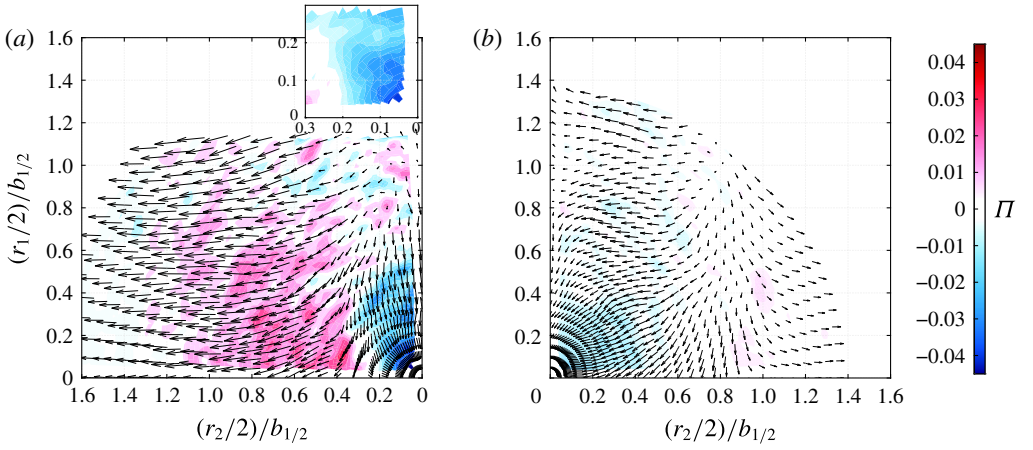


FIGURE 8. Nonlinear interscale energy transfer $\Pi = (\partial \overline{\delta u_k'' (\delta u_i'')^2_\rho})/\partial r_k$ in (a) the air jet and (b) the SF_6 jet at $x_1 = 16d$. The vector field, $\overline{\delta u_k'' (\delta u_i'')^2_\rho}$, is overlaid on the Π colour map. The inset in (a) shows a close-up of Π of the air jet near the origin; the contours are more circular than those of Π_U in figure 7(a), indicating that the nonlinear transfer is more isotropic than the linear transfer.

independent of the inhomogeneous large scales insofar as they only set the dissipation rate. The term Π is therefore amendable to turbulence modelling in that it has the potential of being universal across different flows. To date, it is not known how VD changes Π; a particularly interesting question is whether VD effects will change the scale-invariance property of the energy cascade. We explore the answer to this question below.

Figure 8 shows the normalised nonlinear transfer Π term, and a forward cascade is present in both jets. The air jet in figure 8(a) shows a forward cascade in the axial direction at the small scales, and the magnitudes of the linear and nonlinear transfer terms in the air jet are similar (compare figures 7a and 8a). A closer look at the isocontours near the origin reveals that Π is more isotropic than Π_U, agreeing with observations in figures 5 and 6. The nonlinear term shows a strong inverse cascade among radially aligned eddies larger than $r_2/2 > 0.3b_{1/2}$, a length scale greater than L_{11}.

The SF_6 jet in figure 8(b) has a forward cascade at small scales. A notable difference is seen in the radial eddies, for which the forward cascade extends to larger scales than in the air jet ($r_2/2 = 0.6b_{1/2}$ versus $0.3b_{1/2}$). A possible reason for the greater extent of the forward cascade is that heavy fluid in the SF_6 jet mixes more slowly with the surrounding lighter fluid than in the Boussinesq air jet (Livescu *et al.* 2010), so that the velocities of the heavy fluid decorrelate less rapidly. This supports a more persistent forward cascade over a larger range of scales. The linear and nonlinear transfer terms behave similarly further downstream at $x_1 = 30d$ (not shown).

4.2. *Directionally independent interscale transfer*

The scale-space plot of Π contains both magnitude and directional information. In building turbulence models, the interest is often in specifying the interscale flux across a scale r independent of its orientations. We therefore examine the

https://doi.org/10.1017/jfm.2018.125 Published online by Cambridge University Press

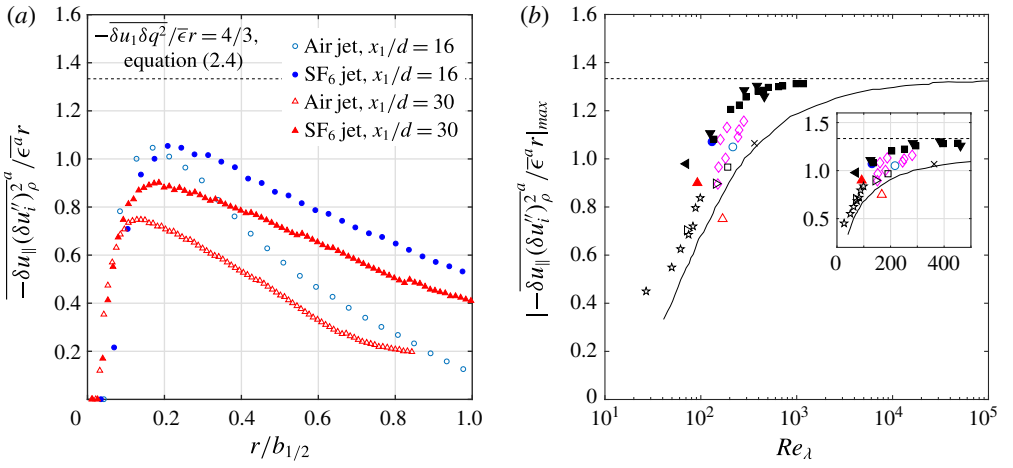


FIGURE 9. Comparison between the measured third-order velocity structure function $\overline{\delta \boldsymbol{u}_\parallel (\delta u_i'')^2_\rho}$ and the prediction by (2.4) in the inertial subrange. (*a*) Present data with air jet data shown as open symbols and SF_6 jet data shown as filled symbols. (*b*) Comparison with round jet data (×) in Burattini *et al.* (2005), 2D wake data (◇) in Thiesset *et al.* (2013), grid turbulence data (⋆) in Zhou & Antonia (2000), (▷) in Gagne *et al.* (2004) and (□) in Van de Water & Herweijer (1999), and forced turbulence data (◀) in Fukayama *et al.* (2000), (▼) in Gotoh, Fukayama & Nakano (2002) and (■) in Moisy, Tabeling & Willaime (1999), together with model predictions (——) by Aivalis *et al.* (2002). For the decaying grid turbulence and forced turbulence datasets, a constant factor of 5/3 is multiplied to the reported data to account for the difference between the 4/5-law and the 4/3-law (2.4). The inset in (*b*) shows the same data points in a linear–linear space to emphasise their behaviour in their range of Re_λ.

orientation-independent nonlinear energy flux below using (2.4). The experimental values are calculated by spherically averaging the vector fields in figure 8 (denoted by $(\cdot)^a$; see the next section). The resulting spherically averaged energy transfer is then a sole function of eddy size $r = |\boldsymbol{r}|$. The curves are then plotted as $-\overline{\delta \boldsymbol{u}_\parallel (\delta u_i'')^2_\rho}^a / \overline{\epsilon}^a r$ against $r/b_{1/2}$ in figure 9(*a*), where the abscissa has been normalised by the velocity half-width $b_{1/2}$ to remove the effect of jet growth. Because the raw dissipation rates contain experimental uncertainties, the dissipation rate used in the above normalisation is obtained from a consideration of satisfying the spherically averaged scale-by-scale energy budget (5.2). This is necessary for a meaningful comparison between the present data and other published datasets. More details of this procedure are given in § 5.2.

The Kolmogorov 4/5-law, or its equivalent form, (2.4), is obtained from the relation $\Pi = -4\overline{\epsilon}$ (2.3) after integration over a sphere of radius r and assuming local isotropy. In the inertial subrange, this yields the equation $\overline{\delta \boldsymbol{u}_\parallel (\delta u_i'')^2_\rho} = -(4/3)\overline{\epsilon} r$ which states a scale-invariant energy cascade since the scale-normalised energy transfer rate, $-\overline{\delta \boldsymbol{u}_\parallel (\delta u_i'')^2_\rho}/\overline{\epsilon} r = 4/3$, is a constant. Strictly speaking, this asymptotic 4/3-state is asserted by Kolmogorov to exist in stationary turbulence (Kolmogorov 1941) when the Reynolds number is sufficiently large and when the local equilibrium hypothesis holds. Whether such a Kolmogorov equilibrium state exists in non-stationary turbulence remains an open question. Even if the equilibrium state does exist, the largest-Re_λ experiments achieved $O(10^3)$ (Warhaft 2009) insinuate that a high Reynolds number

https://doi.org/10.1017/jfm.2018.125 Published online by Cambridge University Press

is necessary, but possibly not sufficient, for attaining equilibrium in non-stationary turbulence. Below, we discuss the variation of scale-normalised energy flux with Re_λ for our experiments, comparing them with other types of equilibrium and non-equilibrium flows.

Figure 9(*a*) shows that the present experiments do not meet the Kolmogorov 4/3 prediction for stationary turbulence. There is a range of scales 0.1–0.3$b_{1/2}$ for which $-\overline{\delta\boldsymbol{u}_{||}(\delta u_i'')_\rho^2}^a/\overline{\epsilon}^a r$ peaks, but at a value lower than 4/3. For example, the air and SF_6 jets at $x_1 = 16d$, having $Re_\lambda = 216$ and 131, have a value of approximately 1.05. So, for both jets, the higher Re_λ are associated with higher transfer rates. The high values of the transfer rates in the heavy jet are related to the strong inverse energy transfer in the linear interscale energy flux term seen in figure 7(*b*) and will be discussed in detail in § 5.4.

To compare the deviations from the Kolmogorov equilibrium state as a function of Re_λ between the present jets and other types of flows, we plot the maximum scale-normalised energy transfer $|-\overline{\delta\boldsymbol{u}_{||}(\delta u_i'')_\rho^2}^a/\overline{\epsilon}^a r|_{max}$ in figure 9(*b*) for (i) a round jet measured at $x_1/d = 40$, (ii) wakes behind 2D bluff bodies of different geometries, (iii) decaying grid turbulence and (iv) forced, stationary and isotropic turbulence in a periodic box. A model prediction of the variation of maximum energy transfer with Re_λ is also included; the predictions are based on a model for the second-order velocity structure function (Aivalis *et al.* 2002), and it approaches the asymptotic 4/3 value for $Re_\lambda \sim 10^5$ (Antonia & Burattini 2006).

The four types of flow listed in the previous paragraph have different trajectories towards the theoretical 4/3 asymptote. The forced turbulence has the fastest trajectory because the turbulence is designed to satisfy Kolmogorov's postulates. The air jet data points and of Burattini *et al.* (2005) are close to the predictions of the Aivalis model. Because the model, and its variants, contains parameters that can be tuned to match a particular flow type (Antonia & Burattini 2006), the reasonably good agreement between its predictions and the jet data suggests that the trend of the jet is consistent, at least with respect to Re_λ. Decaying flows (jets, wakes and grid turbulence) that have the same Re_λ have large variations in the measured maximum scale-normalised energy transfer rate; see, for example, the range $Re_\lambda = 100$–400. This means that universality of turbulence at scales of the order of λ (where $|-\overline{\delta\boldsymbol{u}_{||}(\delta u_i'')_\rho^2}^a/\overline{\epsilon}^a r|_{max}$ occurs) is non-existent at these moderate values of Re_λ as it depends on the flow type. The SF_6 jet data points lie in the same range as the forced turbulence datasets. This occurs because the dense jet turbulence is more 'stationary' with respect to downstream distances x_1 than the Boussinesq air jet; in the range $x_1 = 16d$–$30d$, the t.k.e. of the dense jet decayed by only 20 % whereas the air jet experienced a 44 % reduction (see figure 13 of Charonko & Prestridge (2017)). Hence, the dense jet is closer to stationary turbulence than the air jet. We defer a detailed physical explanation of this peculiar behaviour to § 5.4 after examining the scale-by-scale energy budget of the jet in § 5.2. It may not be possible to develop a generalised model for the dependence of the energy flux on Re_λ for turbulent flows, especially when VD effects are present.

5. Scale-by-scale energy budget

5.1. *Spatial variation of dissipation, production, advection and transport of scale energy*

The analysis of one-point t.k.e. budgets by Charonko & Prestridge (2017) reveals several key differences at the centreline between the air and SF_6 jets. These include (i) negative production, (ii) positive transport and (iii) lower advection. These

https://doi.org/10.1017/jfm.2018.125 Published online by Cambridge University Press

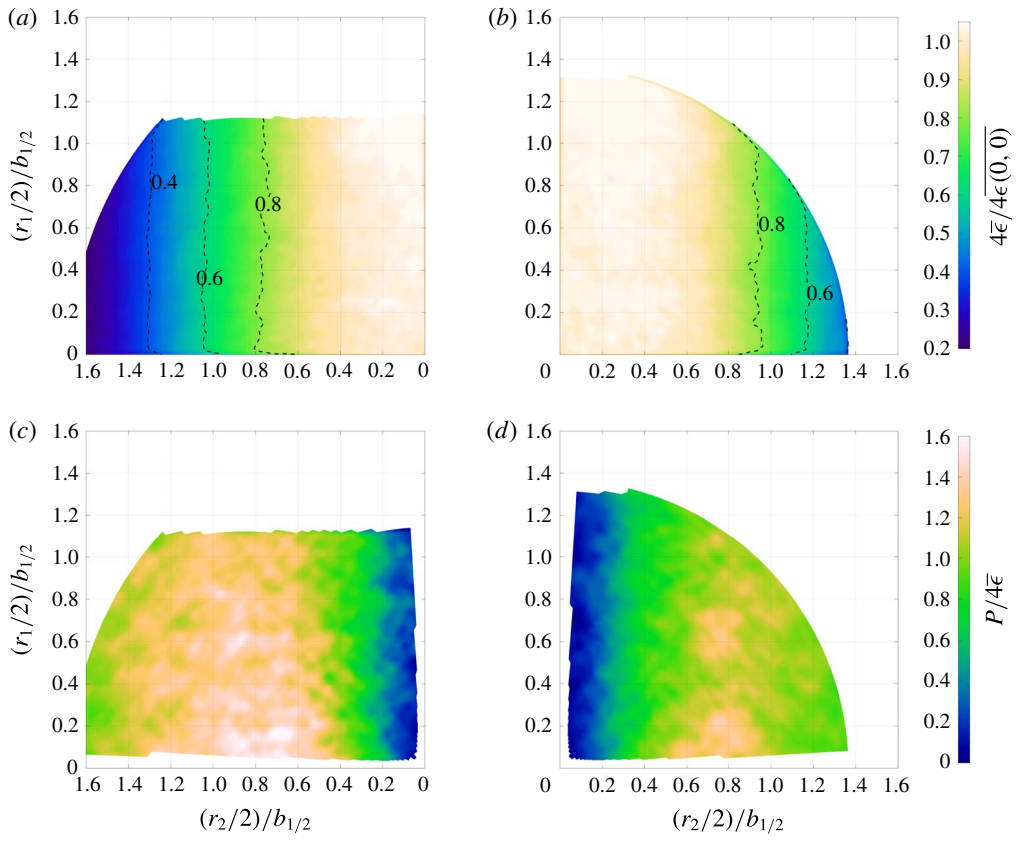


FIGURE 10. Distributions of the dissipation rate (*a*,*b*) and production (*c*,*d*) of scale energy $\overline{(\delta u_i'')^2_\rho}$ in (r_1, r_2)-space for (*a*,*c*) the air jet and (*b*,*d*) the SF_6 jet at $x_1 = 16d$.

observations are further interpreted here using the spatial variation in scale space of the remaining terms appearing in the VD K–H–M equation.

The spatial distributions in (r_1, r_2)-space of $4\overline{\epsilon}$ and P are shown for both jets at $x_1 = 16d$ in figure 10. The plotted dissipation is normalised by the value at the origin, $4\overline{\epsilon(0,0)}$, while P is normalised by the local dissipation $4\overline{\epsilon}$. Figure 10(*a*,*b*) shows that the dissipation varies by less than 20 % for $(r_2/2) < 0.8b_{1/2}$ in both jets, and this region extends to $0.9b_{1/2}$ for the SF_6 jet. The dissipation $4\overline{\epsilon}$ is approximately constant along the streamwise direction r_1, whereas radial gradients are large. The spatial variation of production relative to dissipation (figure 10*c*,*d*) is similar in both jets; $P/(4\overline{\epsilon})$ is low along the jet axis $(r_2/2 < 0.2b_{1/2})$ and reaches its maximum at the shear layer $(r_2/2 = 0.8b_{1/2})$. The peak location can be compared with that of the production term in the t.k.e. budget equation (see figure 15(*a*) in Charonko & Prestridge (2017)). Further, P is positive at the origin for the SF_6 jet, even though the production term in the one-point t.k.e. budget was negative. This apparent contradiction is resolved by recognising that two-point correlations only reduce to their one-point counterparts when r becomes larger than the correlation length scale (Marati *et al.* 2004), e.g. $L_{11} \approx 0.4b_{1/2}$ from table 2. The observation that $P > 0$ for all measured scales here means that the negative production (in the sense of the

https://doi.org/10.1017/jfm.2018.125 Published online by Cambridge University Press

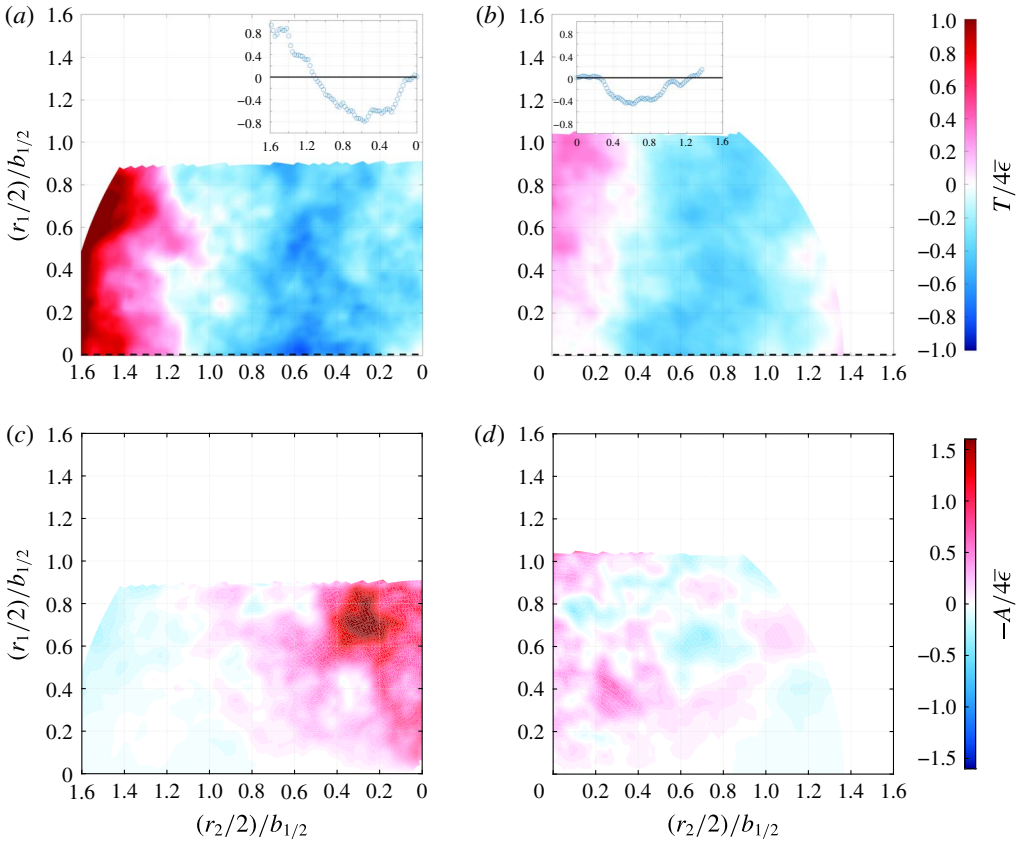


FIGURE 11. Distributions of the transport (*a*,*b*) and advection (*c*,*d*) of scale energy $\overline{(\delta u_i'')^2_\rho}$ in (r_1, r_2)-space for (*a*,*c*) the air jet and (*b*,*d*) the SF_6 jet at $x_1 = 16d$. The insets show a line profile of the distribution along the dotted line for comparison.

one-point t.k.e. budget) is a localised phenomenon because it is confined to a range of scales smaller than L_{11}.

Positive transport and lower advection in the SF_6 jet were observed in the single-point analyses, and figure 11 shows the comparison for the normalised transport term $T/(4\overline{\epsilon})$ and the advection term $-A/(4\overline{\epsilon})$. The insets in the $T/(4\overline{\epsilon})$ plots (*a*,*b*) show a line profile of the quantity as a function of the radial separation r_2 along the dotted line. These line profiles resemble the corresponding term in the single-point t.k.e. equation when r_2 is greater than the flow integral length scale (Marati *et al.* 2004). In both jets, $T/(4\overline{\epsilon})$ crosses zero at approximately $(r_2/2)/b_{1/2} = x_2/b_{1/2} \approx 1.2$ and becomes positive thereafter (see figure 15(*a*) in Charonko & Prestridge (2017)). However, notable differences are seen in the spatial distribution of the transport term. While $T/(4\overline{\epsilon})$ is negative over all measured r_1 separations in the air jet, it is positive in the SF_6 jet, indicating that axially aligned eddies are gaining energy from neighbouring streamwise spatial points. Such transfer is very non-local when compared with the two-point production P. This is consistent with the single-point t.k.e. budget of the SF_6 jet, where the turbulent transport term was measured positive at the jet centreline (Charonko & Prestridge 2017).

https://doi.org/10.1017/jfm.2018.125 Published online by Cambridge University Press

Regarding the distribution of the advection term, $-A/(4\overline{\epsilon})$ in the SF_6 jet is less organised and has smaller magnitudes than in the air jet, probably reflecting the influence of VD effects, and consistent with the lower advection observed in the single-point analysis.

5.2. *Spherically averaged scale-by-scale energy budget*

The VD K–H–M equation (2.7) describes the energy budget at each scale r and quantifies the transfer of energy from the energy-containing large scales to the dissipative small scales, a process of general interest in turbulence modelling. It will be used here to study the role of density variations in the energy cascade. Let us recall the equation in its symbolic form for our time-steady jets,

$$A + \Pi + \Pi_U = P + T + T_p + D_\nu + D_{\boldsymbol{X},\nu} - 4\overline{\epsilon} + a_P - Q. \tag{5.1}$$

As shown in previous figures, the terms in the equation are functions of $(r, \theta; \boldsymbol{X})$, where $r = |\boldsymbol{r}|$. To focus on the interscale energy transfer at each scale r, each of the terms can be spherically averaged, $(\cdot)^a = (2/\pi)\int_0^{\pi/2} F(r, \theta)\,\mathrm{d}\theta$, to remove the orientation (θ) dependence of the scales. After dividing the resultant expression by $4\overline{\epsilon}^a$ on both sides, and also a rearrangement of terms, we obtain the following equation:

$$\overbrace{(P + T + D_\nu + D_{\boldsymbol{X},\nu} + a_P - Q - A - \Pi - \Pi_U)^a/4\overline{\epsilon}^a}^{\text{Measured from data}} + \overbrace{T_p^a/4\overline{\epsilon}^a}^{\text{Modelled}} = \overbrace{1}^{\text{Balance}}. \tag{5.2}$$

The pressure transport term T_p^a could not be measured in the experiments, and it is modelled using Lumley's model (Lumley 1979) as in previous experimental studies (see Charonko & Prestridge (2017) and references therein): $T_p^a = -(2/5)T^a$. The use of Lumley's model is supported by recent DNS data of a constant-density turbulent round jet in Taub *et al.* (2013). In the present context of a two-point statistical equation, the range of applicability of the model is established by considering the asymptotic limit of the K–H–M equation: the equation reduces to the sum of the single-point t.k.e. equations for the two spatial points under consideration when $r > L_{11}$. Because $L_{11} \approx 0.4b_{1/2}$ (see table 2), the asymptotic limit is expected to apply for $r/2 > 0.2b_{1/2}$. Therefore, T_p^a is only computed for this scale range in the budget calculations.

The scale-by-scale budgets for both jets at $x_1 = 16d$ are shown in figure 12. The terms $D_{\boldsymbol{X},\nu}^a$ and Q^a are not shown in the figure because their magnitudes are close to zero at all length scales for both jets. The balance at each r is shown as a black line. The energy balance for both jets is largely flat across all measured r values, indicating that a qualitative balance of (5.2) is achieved. The departure from the exact balance ($\equiv 1$) is explained by the uncertainty in the measured dissipation rate. For the SF_6 jet (figure 12*b*), the balance is much less than one, implying something other than an overestimation of the dissipation by 43 %. The low balance is likely to be due to a combination of uncertainty in dissipation, along with use of the Lumley pressure model for this VD flow. Indeed, the pressure transport term has been shown in the DNS study of Alves Portela *et al.* (2017) to be non-negligible at the small scales, a range that is not accessible in the present jet data. This uncertainty can only be assessed by future resolved numerical simulations.

https://doi.org/10.1017/jfm.2018.125 Published online by Cambridge University Press

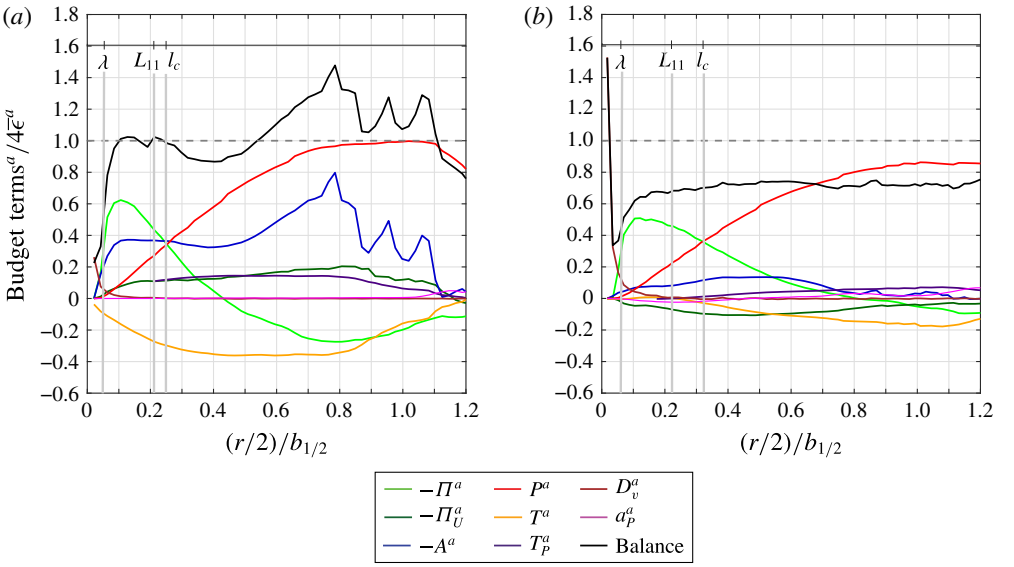


FIGURE 12. The spherically averaged scale-by-scale energy budget (5.2) at $x_1 = 16d$ for (*a*) the air jet and (*b*) the SF_6 jet. The black solid line represents the balance term at each scale r; right-hand side of (5.2). The terms $D^a_{\boldsymbol{X},\nu}$ and Q^a are not shown because the values over these length scales are approximately zero.

A qualitative balance of (5.2) is achieved for both jets in figure 12. To compare the budgets of both jets, we compensate for the systematic uncertainties in the measured dissipation rate by enforcing the constraint expressed by the spherically averaged VD K–H–M equation (5.2), i.e. all terms in the budget are multiplied by the same constant factor to bring the total balance across all scales (black line in figure 12) to a value around one. For the air jet case, there is no correction, since the balance is close to one, whereas it is $1/0.7$ for the SF_6 jet. The dissipation-rate-compensated scale-by-scale energy budgets are shown in figure 13 and their results are used in subsequent discussions on VD effects in jet turbulence.

5.3. *Observations of VD effects in the scale-by-scale budgets*

The common trends in the budget terms between the two jets in figure 13 are that both jets have production (red line) that is small near the centreline, increasing radially. The nonlinear interscale energy transfer (light green line) is positive for both jets near the centreline and peaks for both at $r/2 = 0.1b_{1/2}$. Advection (blue line) is positive for both jets, but the magnitude is much larger in the air jet.

The role of each budget term in (5.2) at a scale r is determined by the sign of each term; positive (negative) terms bring (remove) energy to (from) r. Table 3 gives a summary of the signs of the terms as a function of r. The scale space is divided into two ranges, (i) $\lambda/2 < r/2 < L_{11}/2$ and (ii) $r/2 > l_c/2$, where l_c is known as the cross-over length scale below which the nonlinear interscale energy transfer term begins to dominate over the inhomogeneous terms $-\Pi^a_U$, P^a, T^a, $-A^a$ and $D^a_{\boldsymbol{X},\nu}$ (Thiesset *et al.* 2013). This is determined as the largest value of r between the intersecting curves of $-\Pi$ and the inhomogeneous terms. For both jets, l_c is determined by the intersection between $-\Pi^a$ and P^a; l_c is larger than but of the same order as L_{11} at

https://doi.org/10.1017/jfm.2018.125 Published online by Cambridge University Press

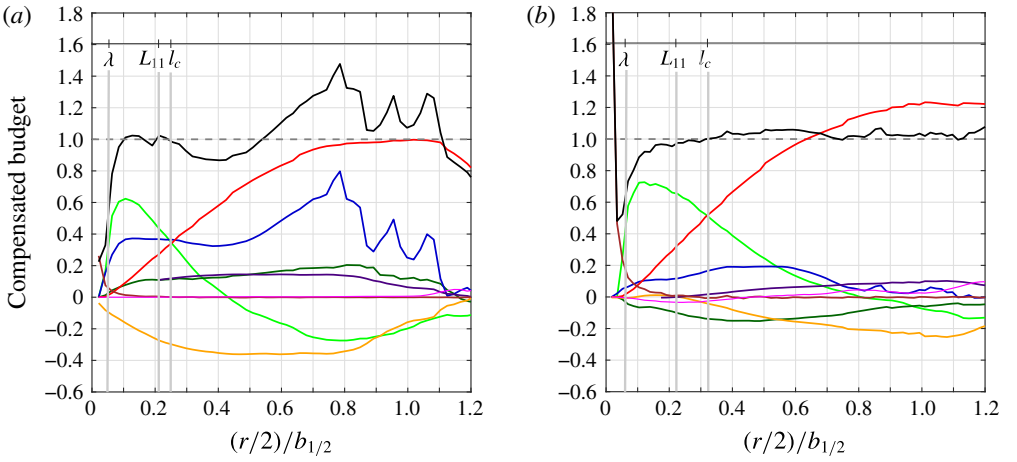


FIGURE 13. The dissipation-rate-compensated spherically averaged scale-by-scale energy budget (5.2) at $x_1 = 16d$ for (*a*) the air jet and (*b*) the SF_6 jet. These budgets compensate for the uncertainties in the measured dissipation rate by enforcing the constraint expressed by the spherically averaged VD K–H–M equation (5.2) on the raw budgets plotted in figure 12 (see the legend therein).

Length scales	$-\Pi^a$	$-\Pi^a_U$	$-A^a$	P^a	T^a	a^a_P	T^a_p
Air jet, $L_{11}/2 = 0.21b_{1/2}$ and $l_c/2 = 0.25b_{1/2}$							
$\lambda/2 < r/2 < L_{11}/2$	+	+	+	+	−	≈ 0	n.a.
$r/2 > l_c/2$	+, −[†]	+	+	+	−	≈ 0	+
SF_6 jet, $L_{11}/2 = 0.22b_{1/2}$ and $l_c/2 = 0.32b_{1/2}$							
$\lambda/2 < r/2 < L_{11}/2$	+	−	+	+	≈ 0	−	n.a.
$r/2 > l_c/2$	+	−	+	+	−	≈ 0	+

TABLE 3. The roles of the scale-by-scale energy budget terms in (5.2) as functions of the scale r, integral length scale L_{11} and cross-over length scale l_c. A '+' ('−') term indicates that the scale r is gaining (losing) energy due to the term. The pressure transport term T^a_p is estimated as $-0.4 \times -T^a$ (see the discussion in the text). The terms D^a_ν, $D^a_{X,\nu}$ and Q^a are not shown because the values over these length scales are approximately zero.

[†] $-\Pi^a$ changes sign at $r/2 = 0.4b_{1/2}$.

the jet centreline. The scales l_c, L_{11} and λ are all marked on the graphs in figure 13 for reference.

In the air jet, scales smaller than L_{11} obtain their energies from both interscale energy transfer terms, the advection term and the production term, while the turbulent flux term, T^a, removes energy from them. For scales larger than l_c, all but the nonlinear interscale transfer term retain their roles; $-\Pi^a$ changes sign at $r/2 > 0.4b_{1/2}$ and becomes negative, in agreement with the strong inverse cascade observed for radially aligned eddies in figure 8(*a*). The VD terms, a^a_P and Q^a, are essentially zero across all measured scales in the Boussinesq air jet. The viscous diffusion terms, D^a_ν and $D^a_{X,\nu}$, are also zero; the former is only significant for scales smaller than λ and will be discussed later, whereas the latter is negligible.

https://doi.org/10.1017/jfm.2018.125 Published online by Cambridge University Press

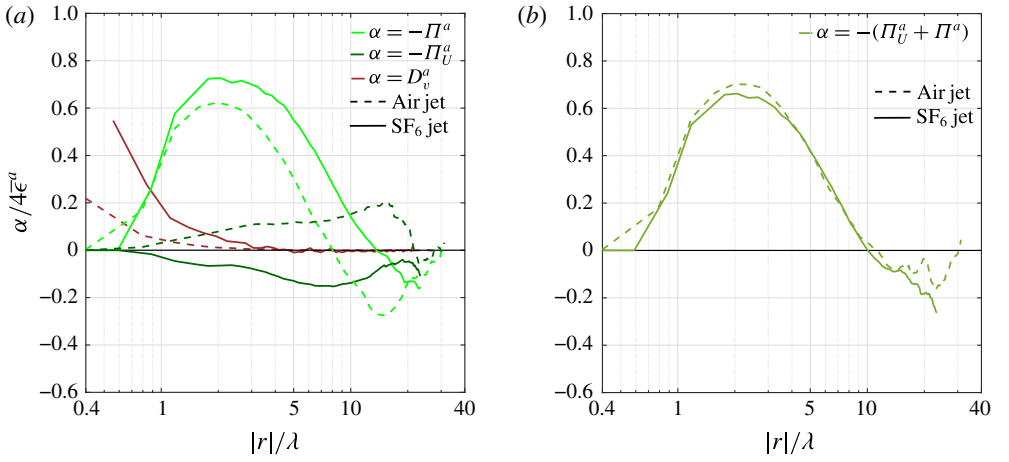


FIGURE 14. The dissipation-rate-compensated spherically averaged (*a*) interscale energy transfer terms and viscous diffusion term and (*b*) sum of interscale energy transfer terms as a function of the normalised scale r/λ at $x_1 = 16d$.

Several significant differences exist in the scale-by-scale energy budget of the VD SF_6 jet (figure 13*b*).

(i) The zero-crossing length scale of the nonlinear interscale energy transfer term (light green line) is larger than that of the air jet, and the value after the zero crossing remains close to zero, suggesting that VD effects dampen the formation of an inverse energy cascade.

(ii) A negative linear interscale energy transfer term (dark green line) throughout the range of measured scales.

(iii) A non-negligible mass-flux–pressure term, a^a_P (pink line), for scales smaller than L_{11}.

(iv) An essentially zero turbulent flux term (orange line) for the small scales.

To emphasise the behaviour at small scales, figure 14 plots the normalised $-\Pi^a$, $-\Pi^a_U$ and D^a_ν from both jets as a function of r/λ. The terms $-\Pi^a$ and D^a_ν are singled out here because they are responsible for energy transfer in $\boldsymbol{r}$-space and only implicitly depend on the inhomogeneous large scales. They therefore have the best potential to be modelled by a universal form. For both jets, $-\Pi^a/4\overline{\epsilon}^a$ reaches its peak value (0.62 for air and 0.73 for SF_6 in figure 14*a*) at $r/\lambda = 1.5$–2.0 and decreases much faster to the left of the peak than the right. This can be compared with the decaying grid turbulence data in Valente & Vassilicos (2015) (figure 10 in that paper), where $-\Pi^a/4\overline{\epsilon}^a|_{max} = 0.55$ at $r/\lambda \approx 1$ for the range of local Reynolds number $Re_\lambda \in [80, 100]$. The viscous diffusion term $D^a_\nu/4\overline{\epsilon}^a$ only becomes significant for $r/\lambda < 1$ because of its role in the final viscous dissipation of $\overline{(\delta u_i'')^2_\rho}$. The smallest resolved scale in the present PIV data is approximately 12η (Nyquist criterion) and is therefore not sufficient to resolve further rise of the term as $r \to \eta$. The dense jet has a larger $D^a_\nu/4\overline{\epsilon}^a$ term than the Boussinesq air jet because $a^a_P/4\overline{\epsilon}^a$ and $\Pi^a_U/4\overline{\epsilon}^a$ are both negative in the inertial subrange ($\lambda < |r| < L_{11}$), causing the $D^a_\nu/4\overline{\epsilon}^a$ term to rise earlier. The $a^a_P/4\overline{\epsilon}^a$ term is a VD effect that is absent in constant-density flows.

The linear transfer term is of opposite sign between the jets, but about the same magnitude. The result is that the total interscale energy flux $-(\Pi_U + \Pi)^a$, plotted

https://doi.org/10.1017/jfm.2018.125 Published online by Cambridge University Press

in figure 14(*b*), is very similar for both jets. The negative linear term of the dense jet compensates for the increased nonlinear term. When $|r| < \lambda$, the nonlinear terms in both jets have very similar profiles, reflecting the small contribution by the inhomogeneous $-\Pi_U^a$ term at these small dissipative scales.

A significant difference between the jets is that the SF_6 jet has a larger range of scales r with $-\Pi/4\overline{\epsilon}^a \approx$ constant. This agrees with the earlier discussion of figure 8 that heavy fluid packets mix more slowly with their lighter surroundings, and hence the velocities of heavy fluids decorrelate more slowly than those of fluids with similar densities undergoing mixing (Dimotakis 1986; Chassaing, Harran & Joly 1994; Charonko & Prestridge 2017). Density variations aid in the creation of an inertial subrange that has, by definition, a constant energy flux independent of scales. On top of this extended inertial subrange, another feature is that the dense jet has a larger maximum normalised nonlinear interscale energy flux, already noted in figure 9, despite having a lower Re_λ than the air jet (table 2). An explanation for this observation is given in the next subsection.

5.4. *Discussion of VD energy cascade*

Now that we understand the roles of each of the budget terms and their relationship to the length scales in the flow, the energetics at the jet centreline can be better understood. The energy cascade of the Boussinesq air jet is similar to a homogeneous shear flow. This can be appreciated by three observations.

(i) The net interscale energy transfer $-(\Pi_U^a + \Pi^a)$ is approximately zero for $r/2 > 0.8b_{1/2}$, whereas it is greater than zero for $r/2 < 0.8b_{1/2}$.

(ii) The sum of the inhomogeneous advection and turbulent transport terms $(T^a - A^a)$ is approximately zero for a broad range of scales. A similar observation is reported from a DNS study of the near wake behind a square prism (Alves Portela *et al.* 2017); the authors found that a balance progressively develops downstream from the location of the turbulent intensity peak which is less than two prism diameters away from the prism. Gomes-Fernandes *et al.* (2015) also reported such balance in the t.k.e. production region of fractal-grid-generated turbulence. It then appears that this is characteristic of turbulence with a mean flow; our Boussinesq jet and the planar wake are decaying turbulence, whereas the fractal-grid turbulence is still strengthening. The approximate balance suggests that the sweeping decorrelation hypothesis (Tsinober 2009), which is closely related to but not exactly the same as Taylor's frozen turbulence hypothesis, is valid at the air jet centreline. The hypothesis asserts that the small-scale turbulent eddies are advected by the larger turbulent eddies (mean flow), during which they experience no dynamical decay. Kholmyansky & Tsinober (2008) give a detailed test of the validity of this hypothesis in the atmospheric boundary layer using several exact kinematic relations involving terms like $\overline{(\underline{u_i} + \underline{u_i})^2(\underline{u_i} - \underline{u_i})}$.

(iii) The production is a major term (accounting for over 80 %) that balances dissipation ($P^a \approx \overline{\epsilon}^a$) at the large scales (for $r/2 > 0.6b_{1/2}$). The remaining 20 % or less of the energy balance is supplied by the net contribution between advection, turbulent transport and pressure transport.

A simplified budget that is accurate to within 20 % for the Boussinesq jet is therefore $-(\Pi_U^a + \Pi^a) + P^a \approx \overline{\epsilon}^a$. This expression states that production at the large scales, where the interscale energy flux is negligible, sets the rate of turbulent dissipation ($P^a \approx \overline{\epsilon}^a$); the variations of $\overline{\epsilon}$ are within 20 % of the centreline value, as

https://doi.org/10.1017/jfm.2018.125 Published online by Cambridge University Press

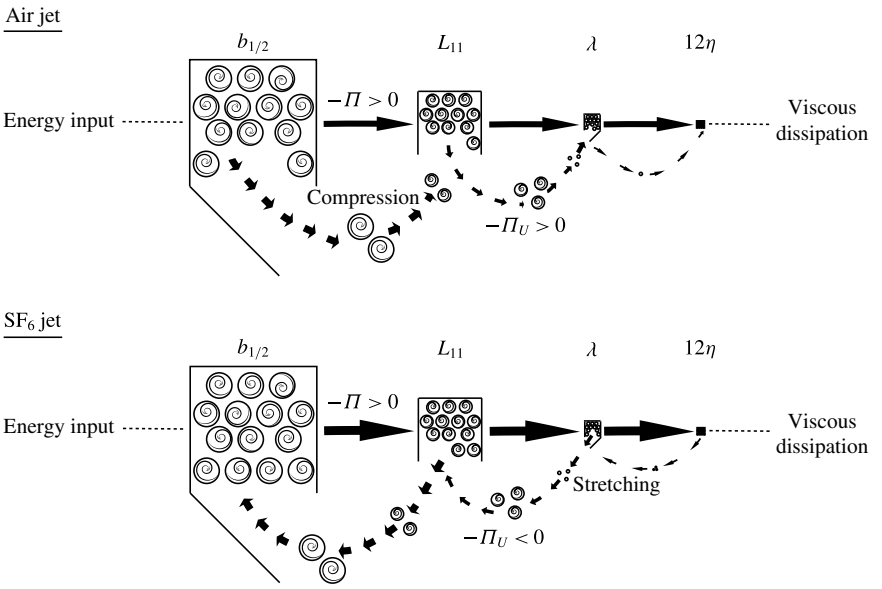


FIGURE 15. A representation of the interscale energy transfer in the air and SF_6 jets. The line thicknesses of the arrows are scaled with respect to the actual magnitudes of $-\Pi_U$ and $-\Pi$ shown in figure 14; a thicker arrow represents a larger energy transfer. The eddy sizes are also drawn to scale, and 12η is the smallest resolved scale in the experiments.

shown in figure 10 for $r/2 < 0.8b_{1/2}$. This injected energy cascades down the scales with a diminishing production term. This simplified picture is complicated by an insufficiently large Re_λ, where inhomogeneities ($-\Pi_U^a$, $-A^a$, T^a, P^a) contaminate the cascade. The energy cascade model of the air jet is shown in figure 15.

In contrast to the air jet, the non-Boussinesq SF_6 jet exhibits a retarded total energy transfer caused by a negative linear interscale energy transfer term at all scales. A model of the energy transfer mechanisms in the SF_6 jet is illustrated in figure 15. There are important ways in which the dense jet differs from the Boussinesq jet.

(i) The simplified budget for the air jet is $-(\Pi_U^a + \Pi^a) + P^a \approx \overline{\epsilon}^a$, with the interscale energy transfer terms being of the same sign at smaller scales. For the SF_6 jet, the simplified budget is $-\Pi^a + P^a \approx \Pi_U^a + \overline{\epsilon}^a$. At scales larger than the Kolmogorov scale, Π_U^a causes energy to be moved from small scales to large through distortion and stretching of eddies. This can be thought of as a mechanism of 'pseudodissipation', in that energy is being removed from the flow. It is unlike dissipation occurring at the Kolmogorov length scales because, as figure 7 shows, the negative value of $-\Pi_U$ reflects the redistribution of scale energy from small off-axis eddies to larger ones oriented away from the streamwise direction, and it occurs at length scales greater than η.

(ii) To maintain the balance of the energy budget at each scale, the $-\Pi^a/4\overline{\epsilon}^a$ term is larger in the dense jet, increasing the forward energy cascade. This is the reason why in figure 9(*b*) the data point of the SF_6 jet at $x_1 = 16d$ lies away from those of the air jet and of other datasets. We can quantify the magnitude of the pseudodissipation mechanism by looking at $-\Pi_U^a/4\overline{\epsilon}^a$ and $P^a/4\overline{\epsilon}^a$ in the energy budget at the large scales in figure 13(*b*). For $(r/2) > 0.65b_{1/2}$, the production

https://doi.org/10.1017/jfm.2018.125 Published online by Cambridge University Press

of scale energy or t.k.e. is 20 % higher than the required dissipation, and this extra production is removed by a combination of the transport and the $-\Pi_U^a/4\overline{\epsilon}^a$ term. Physically, this means that not all of the scale energy production is made available to sustain and create turbulent fluctuations; 4–5 % of it is immediately fed back to the mean flow (large eddies) by the linear interscale energy flux term which distorts turbulent eddies into larger ones, as seen in figure 7(*b*). This leads to the slower centreline jet velocity decay and a smaller jet growth rate observed for the SF_6 jet (Charonko & Prestridge 2017). This also identifies the deformation of eddies into larger ones as the physical mechanism through which the observed negative t.k.e. production at the jet centreline is affected. The energy cascade, measured by the nonlinear interscale energy flux, has no role in the process but is enhanced by VD effects to maintain the energy balance at each scale. In figure 15, the eddy size and the magnitudes of the transfer terms are drawn to scale, with the latter represented by the line thickness of the arrows.

(iii) Another mechanism in the dense jet that strengthens the mean flow at the expense of fluctuations is the mass-flux–pressure term a_P^a. The term a_P acts as the link between the equations of Favre-mean kinetic energy $(\tilde{U}_i\tilde{U}_i)/2$ and Favre-averaged turbulent kinetic energy $(\widetilde{u_i''u_i''})/2$. It being negative at the small scales means that energy is transferred (lost) from the fluctuations to the mean flow (Livescu & Ristorcelli 2007), so it reinforces the mean flow and again leads to a smaller decay constant for the centreline velocity (Charonko & Prestridge 2017). As a consequence, a_P is also retarding the energy cascade, but it has a smaller magnitude than $-\Pi_U$.

(iv) The final difference from the Boussinesq air jet is that the advection term and turbulent transport term are no longer in balance, and this is true for scales smaller than l_c, which contribute most to the velocity gradient. This implies that the sweeping decorrelation hypothesis may not be valid at the centreline of the dense jet (see point (ii) for the air jet, above).

Overall, jet turbulence at the centreline for the present jets with finite Reynolds numbers is not in Richardson–Kolmogorov equilibrium, i.e. strict satisfaction of (2.3). Contributions from the inhomogeneous terms $(P + T - \Pi_U - A)^a$ are comparable in magnitude to the nonlinear energy flux Π^a. Such a departure is usually attributed to finite-Reynolds-number effects (as shown in figure 9). Valente & Vassilicos (2015) pointed out that this can also be caused by different types of spectral imbalances that may persist in some manner at high Reynolds numbers.

A possible approach to modelling the retarded total energy transfer in the VD jet is through the subgrid-scale dissipation $2\nu_T\overline{S_{ij}}\,\overline{S_{ij}}$, where $\overline{S_{ij}}$ is the resolved instantaneous rate-of-strain tensor. For wall-bounded turbulent flows, Lévêque *et al.* (2007) proposed an improved Smagorinsky model with the eddy viscosity specified as $\nu_T = (C_s\Delta)^2(|\overline{\boldsymbol{S}}| - |\langle\overline{\boldsymbol{S}}\rangle|)$, where $\langle\overline{\boldsymbol{S}}\rangle$ is the resolved mean shear, $|\cdot|$ denotes the magnitude of the second-order tensor and $C_s = 0.16$ is the standard Smagorinsky constant. Their model can be regarded as a sum of the standard Smagorinsky model and a second part $(C_s\Delta)^2(-|\langle\overline{\boldsymbol{S}}\rangle|)$ representing the effect of mean shear on the energy cascade. This prescription can be interpreted as $-(\Pi + \Pi_U)$, wherein the nonlinear interscale energy transfer term is represented by the standard Smagorinsky model. Comparison between the predictions of this model and of DNS by Moser, Kim & Mansour (1999) shows that the first- and second-order velocity statistics are in close agreement across the whole wall layer. The model also exhibits the correct scaling behaviour for the interscale energy flux when either the fluctuating strains (in the bulk

https://doi.org/10.1017/jfm.2018.125 Published online by Cambridge University Press

region) or the mean shear (in the near-wall region) dominate. A simple extension of the model to allow for the observed inverse energy transfer in Π_U of the SF_6 jet is to flip the sign of the mean shear (second) term, i.e. $(C_s\Delta)^2(|\langle\overline{\boldsymbol{S}}\rangle|)$. Hence, this represents a retarded energy transfer. In practical calculations where the sign of Π_U is unknown *a priori*, Π_U can be computed from the resolved fields of velocity and density, and the sign of $(C_s\Delta)^2(|\langle\overline{\boldsymbol{S}}\rangle|)$ can be determined subsequently. This proposal needs to be assessed in future numerical simulations.

6. Conclusions

By extending the original K–H–M equation for constant-density flows to include VD effects (2.7) and applying it to an experimental dataset, we are able to make several new observations about the effects of VD on the energy cascade and the total interscale energy transfer.

(i) Density variations aid the development of a scale-invariant inertial subrange in terms of both the range of scales and the magnitude.

(ii) In the absence of shocks, the final viscous dissipation of t.k.e. in high-Reynolds-number VD flows is the same as in constant-density flows (2.9).

(iii) Negative t.k.e. production observed at the SF_6 jet centreline leads to strong inverse energy transfer in the linear interscale energy transfer term Π_U over all length scales measured in the flow. Total negative production occurs over a narrow range of scales smaller than the integral length scale L_{11}.

(iv) Strong density variations at the SF_6 jet centreline inhibit the turbulent transport of scale energy in physical space for scales smaller than L_{11}. This leads to imbalance of the sum $(T^a - A^a)$ and suggests the inapplicability of the sweeping decorrelation hypothesis at the jet centreline.

Further experimental and numerical work is needed to validate the approximations and assumptions made in § 3.3 when (2.7) was evaluated from our planar laboratory data. At present, no DNS dataset is available for a SF_6 jet that has a density ratio near four. There is also no volumetric experimental dataset that permits us to check our approximations and assumptions. To advance our understanding of the fine-scale kinematics of VD jets, we are currently setting up a combined stereoscopic PLIF/PIV system at a jet cross-section for the same jets as reported in this paper. Together with Taylor's frozen turbulence hypothesis, we will be able to obtain pseudovolumetric data for the jets.

Acknowledgement

We would like to thank T. Clark for his fruitful discussions on the theoretical aspects of this work.

Appendix A

This appendix presents a derivation of the K–H–M equation under VD settings. Employing the Favre-averaged (mass-weighted) formalism, the decomposition of instantaneous velocity at the two separate spatial points $\boldsymbol{x}$ and $\boldsymbol{x}'$ can be written as $u_i(\boldsymbol{x}) = \underline{U_i} + \underline{u_i'} = \underline{\tilde{U}_i} + \underline{u_i''}$ and $u_i(\boldsymbol{x}') = \underline{\underline{U_i}} + \underline{\underline{u_i'}} = \underline{\underline{\tilde{U}_i}} + \underline{\underline{u_i''}}$. A tilde denotes a

https://doi.org/10.1017/jfm.2018.125 Published online by Cambridge University Press

Favre-averaged quantity, $\tilde{\phi} = \overline{\rho\phi}/\overline{\rho}$, and ϕ'' is the remaining Favrian fluctuation. The densities are $\rho(\boldsymbol{x}) = \underline{\rho}$ and $\rho(\boldsymbol{x}') = \underline{\underline{\rho}}$ respectively. As discussed in § 2, $\overline{(\delta u_i'')^2_\rho}$ (2.6) is the appropriate definition of scale energy in VD flows. The evolution equation of interscale energy transfer can then be obtained from the components, $\underline{R_{ii}}$, $\underline{\underline{R_{ii}}}$ and $R_{ii}(\boldsymbol{x}, \boldsymbol{x}') = (1/2)\overline{[\rho(\boldsymbol{x}) + \rho(\boldsymbol{x}')]u_i''(\boldsymbol{x})u_i''(\boldsymbol{x}')}$. A self-contained development of the equation is given below. The approximations and mathematical relations employed are listed below.

(i) Coordinate transform – $\partial/\partial\underline{x_k} = \partial/\partial r_k + (\partial/\partial X_k)/2$ and $\partial/\partial\underline{\underline{x_k}} = -(\partial/\partial r_k) + (\partial/\partial X_k)/2$.

(ii) Independence of variables – $\partial\underline{u_k''}/\partial\underline{\underline{x_i}} = \partial\underline{\underline{u_k''}}/\partial\underline{x_i} = 0$, etc.

(iii) Divergence-free Favre-mean and fluctuating velocities – $\partial\underline{\tilde{U}_k}/\partial\underline{x_k} \approx 0$ and $\partial\underline{u_k''}/\partial\underline{x_k} \approx 0$.

(iv) Commutativity of differential and ensemble (time-) averaging operator – $\overline{\partial(\cdot)/\partial\underline{x_k}} = \partial\overline{(\cdot)}/\partial\underline{x_k}$.

$\underline{R_{ii}} = R_{ii}(\boldsymbol{x}) = \overline{\rho(\boldsymbol{x})u_i''^2(\boldsymbol{x})}$:

$$\frac{\partial\underline{R_{ii}}}{\partial t} + \frac{\partial\underline{\tilde{U}_k R_{ii}}}{\partial\underline{x_k}} + \frac{\partial\underline{R_{iik}}}{\partial\underline{x_k}} + 2\underline{R_{ik}}\frac{\partial\underline{\tilde{U}_i}}{\partial\underline{x_k}} = 2\overline{\underline{u_i'}\frac{\partial\underline{\sigma_{ik}'}}{\partial\underline{x_k}}} - 2\underline{a_i}\frac{\partial\underline{\overline{\sigma_{ik}}}}{\partial\underline{x_k}}. \tag{A 1}$$

$\underline{\underline{R_{ii}}} = R_{ii}(\boldsymbol{x}') = \overline{\rho(\boldsymbol{x}')u_i''^2(\boldsymbol{x}')}$:

$$\frac{\partial\underline{\underline{R_{ii}}}}{\partial t} + \frac{\partial\underline{\underline{\tilde{U}_k R_{ii}}}}{\partial\underline{\underline{x_k}}} + \frac{\partial\underline{\underline{R_{iik}}}}{\partial\underline{\underline{x_k}}} + 2\underline{\underline{R_{ik}}}\frac{\partial\underline{\underline{\tilde{U}_i}}}{\partial\underline{\underline{x_k}}} = 2\overline{\underline{\underline{u_i'}}\frac{\partial\underline{\underline{\sigma_{ik}'}}}{\partial\underline{\underline{x_k}}}} - 2\underline{\underline{a_i}}\frac{\partial\underline{\underline{\overline{\sigma_{ik}}}}}{\partial\underline{\underline{x_k}}}. \tag{A 2}$$

$R_{ii}(\boldsymbol{x}, \boldsymbol{x}') = \frac{1}{2}\overline{[\rho(\boldsymbol{x}) + \rho(\boldsymbol{x}')]u_i''(\boldsymbol{x})u_i''(\boldsymbol{x}')} = \frac{1}{2}\overline{[\underline{\rho} + \underline{\underline{\rho}}]\underline{u_i''}\,\underline{\underline{u_i''}}}$:

$$\begin{aligned}
&\frac{\partial R_{ii}}{\partial t} + \frac{\partial\underline{\tilde{U}_k}R_{ii}}{\partial\underline{x_k}} + \frac{\partial\underline{\underline{\tilde{U}_k}}R_{ii}}{\partial\underline{\underline{x_k}}} + \frac{\partial R_{iik}(\boldsymbol{x}, \boldsymbol{x}', \boldsymbol{x})}{\partial\underline{x_k}} + \frac{\partial R_{iik}(\boldsymbol{x}, \boldsymbol{x}', \boldsymbol{x}')}{\partial\underline{\underline{x_k}}} \\
&\quad - \frac{1}{2}\{T_{ii}(\boldsymbol{x}, \boldsymbol{x}') + T_{ii}(\boldsymbol{x}', \boldsymbol{x})\} \\
&\quad + R_{ki}\frac{\partial\underline{\tilde{U}_i}}{\partial\underline{x_k}} + R_{ik}\frac{\partial\underline{\underline{\tilde{U}_i}}}{\partial\underline{\underline{x_k}}} - \frac{Q_i(\boldsymbol{x}, \boldsymbol{x}')}{\underline{\underline{\rho}}}\frac{\partial\underline{\underline{R_{ik}}}}{\partial\underline{\underline{x_k}}} - \frac{Q_i(\boldsymbol{x}', \boldsymbol{x})}{\underline{\rho}}\frac{\partial\underline{R_{ik}}}{\partial\underline{x_k}} \\
&\quad = -a_i(\boldsymbol{x}, \boldsymbol{x}')\frac{\partial\underline{\underline{\overline{\sigma_{ik}}}}}{\partial\underline{\underline{x_k}}} - a_i(\boldsymbol{x}', \boldsymbol{x})\frac{\partial\underline{\overline{\sigma_{ik}}}}{\partial\underline{x_k}} + \Omega_{ii}(\boldsymbol{x}, \boldsymbol{x}') + \Omega_{ii}(\boldsymbol{x}', \boldsymbol{x}).
\end{aligned} \tag{A 3}$$

Here,

(i) $T_{ij}(\boldsymbol{x}, \boldsymbol{x}') = \overline{\rho(\boldsymbol{x})u_i''(\boldsymbol{x})u_j''(\boldsymbol{x}')(\partial\underline{\underline{u_k}}/\partial\underline{\underline{x_k}})}$,

(ii) $Q_i(\boldsymbol{x}, \boldsymbol{x}') = (\overline{[\rho(\boldsymbol{x}) + \rho(\boldsymbol{x}')]u_i''(\boldsymbol{x})})/2 = (\overline{\rho(\boldsymbol{x}')u_i''(\boldsymbol{x})})/2$,

(iii) $a_i(\boldsymbol{x}, \boldsymbol{x}') = -(1/2)\{\overline{\rho(\boldsymbol{x})u_i''(\boldsymbol{x})/\rho(\boldsymbol{x}')} + \overline{u_i''(\boldsymbol{x})} - \overline{\rho(\boldsymbol{x}')u_i''(\boldsymbol{x})}/\overline{\rho(\boldsymbol{x}')}\}$,

(iv) $\Omega_{ij}(\boldsymbol{x}, \boldsymbol{x}') = -\Pi_{ij}(\boldsymbol{x}, \boldsymbol{x}') - E_{ij}(\boldsymbol{x}, \boldsymbol{x}')$,

(v) $\Pi_{ij}(\boldsymbol{x}, \boldsymbol{x}') = \{\overline{[1 + \rho(\boldsymbol{x})/\rho(\boldsymbol{x}')]u_i''(\boldsymbol{x})(\partial p'(\boldsymbol{x}')/\partial\underline{\underline{x_j}})}\}/2$,

https://doi.org/10.1017/jfm.2018.125 Published online by Cambridge University Press

(vi) $E_{ij}(\boldsymbol{x},\boldsymbol{x}') = -(1/2)\{\overline{[1+\rho(\boldsymbol{x})/\rho(\boldsymbol{x}')]u_i''(\boldsymbol{x})(\partial\tau'_{jk}(\boldsymbol{x}')/\partial\underline{\underline{x_k}})}\}$,

(vii) $R_{iik}(\boldsymbol{x},\boldsymbol{x}',\boldsymbol{x}) = (1/2)\overline{[\rho(\boldsymbol{x})+\rho(\boldsymbol{x}')]u_i''(\boldsymbol{x})u_i''(\boldsymbol{x}')u_k''(\boldsymbol{x})}$,

(viii) $R_{iik}(\boldsymbol{x},\boldsymbol{x}',\boldsymbol{x}') = (1/2)\overline{[\rho(\boldsymbol{x})+\rho(\boldsymbol{x}')]u_i''(\boldsymbol{x})u_i''(\boldsymbol{x}')u_k''(\boldsymbol{x}')}$.

Temporal term:

$$\frac{\partial}{\partial t}(\underline{R_{ii}} + \underline{\underline{R_{ii}}} - 2R_{ii}(\boldsymbol{x},\boldsymbol{x}')) = \frac{\partial\overline{(\delta u_i'')^2_\rho}}{\partial t}. \tag{A 4}$$

Linear advection term:

$$\begin{aligned}
&\frac{\partial\underline{\tilde{U}_k R_{ii}}}{\partial\underline{x_k}} + \frac{\partial\underline{\underline{\tilde{U}_k R_{ii}}}}{\partial\underline{\underline{x_k}}} - 2\frac{\partial\underline{\tilde{U}_k R_{ii}}}{\partial\underline{x_k}} - 2\frac{\partial\underline{\underline{\tilde{U}_k R_{ii}}}}{\partial\underline{\underline{x_k}}} \\
&\quad= \frac{\partial}{\partial\underline{x_k}}[\underline{\tilde{U}_k}(\overline{(\delta u_i'')^2_\rho} - \underline{\underline{R_{ii}}})] + \frac{\partial}{\partial\underline{\underline{x_k}}}[\underline{\underline{\tilde{U}_k}}(\overline{(\delta u_i'')^2_\rho} - \underline{R_{ii}})] \\
&\quad= \underline{\tilde{U}_k}\frac{\partial\overline{(\delta u_i'')^2_\rho}}{\partial\underline{x_k}} + \underline{\underline{\tilde{U}_k}}\frac{\partial\overline{(\delta u_i'')^2_\rho}}{\partial\underline{\underline{x_k}}} \\
&\quad= \underline{\tilde{U}_k}\left\{\frac{\partial}{\partial r} + \frac{1}{2}\frac{\partial}{\partial X_k}\right\}\overline{(\delta u_i'')^2_\rho} + \underline{\underline{\tilde{U}_k}}\left\{-\frac{\partial}{\partial r} + \frac{1}{2}\frac{\partial}{\partial X_k}\right\}\overline{(\delta u_i'')^2_\rho} \\
&\quad= \frac{(\underline{\tilde{U}_k} + \underline{\underline{\tilde{U}_k}})}{2}\frac{\partial\overline{(\delta u_i'')^2_\rho}}{\partial X_k} + \frac{\partial(\underline{\tilde{U}_k} - \underline{\underline{\tilde{U}_k}})\overline{(\delta u_i'')^2_\rho}}{\partial r_k}.
\end{aligned} \tag{A 5}$$

Nonlinear advection term:

$$\begin{aligned}
&\frac{\partial\underline{R_{iik}}}{\partial\underline{x_k}} + \frac{\partial\underline{\underline{R_{iik}}}}{\partial\underline{\underline{x_k}}} - 2\frac{\partial R_{iik}(\boldsymbol{x},\boldsymbol{x}',\boldsymbol{x})}{\partial\underline{x_k}} - 2\frac{\partial R_{iik}(\boldsymbol{x},\boldsymbol{x}',\boldsymbol{x}')}{\partial\underline{\underline{x_k}}} \\
&\quad= \frac{\partial}{\partial\underline{x_k}}[\overline{\underline{u_k''}(\delta u_i'')^2_\rho} - \overline{\underline{\underline{\rho u_i''^2 u_k''}}}] + \frac{\partial}{\partial\underline{\underline{x_k}}}[\overline{\underline{\underline{u_k''}}(\delta u_i'')^2_\rho} - \overline{\underline{\rho u_i''^2}\,\underline{\underline{u_k''}}}] \\
&\quad= \frac{\partial\overline{(\underline{u_k''} - \underline{\underline{u_k''}})(\delta u_i'')^2_\rho}}{\partial r_k} + \frac{1}{2}\frac{\partial\overline{(\underline{u_k''} + \underline{\underline{u_k''}})(\delta u_i'')^2_\rho}}{\partial X_k}.
\end{aligned} \tag{A 6}$$

Production term:

$$\begin{aligned}
&2\underline{R_{ik}}\frac{\partial\underline{\tilde{U}_i}}{\partial\underline{x_k}} + 2\underline{\underline{R_{ik}}}\frac{\partial\underline{\underline{\tilde{U}_i}}}{\partial\underline{\underline{x_k}}} - 2R_{ki}\frac{\partial\underline{\tilde{U}_i}}{\partial\underline{x_k}} - 2R_{ik}\frac{\partial\underline{\underline{\tilde{U}_i}}}{\partial\underline{\underline{x_k}}} \\
&\quad= 2\left\{(\underline{R_{ik}} - R_{ki})\frac{\partial(\underline{\tilde{U}_i} - \underline{\underline{\tilde{U}_i}})}{\partial\underline{x_k}} + (\underline{\underline{R_{ik}}} - R_{ik})\frac{\partial(\underline{\underline{\tilde{U}_i}} - \underline{\tilde{U}_i})}{\partial\underline{\underline{x_k}}}\right\} \\
&\quad= 2[(\underline{R_{ik}} - R_{ki}) + (\underline{\underline{R_{ik}}} - R_{ik})]\frac{\partial(\underline{\tilde{U}_i} - \underline{\underline{\tilde{U}_i}})}{\partial r_k} + [(\underline{R_{ik}} - R_{ki}) - (\underline{\underline{R_{ik}}} - R_{ik})]\frac{\partial(\underline{\tilde{U}_i} - \underline{\underline{\tilde{U}_i}})}{\partial X_k} \\
&\quad= 2[A_{ik} + B_{ik}]\frac{\partial(\underline{\tilde{U}_i} - \underline{\underline{\tilde{U}_i}})}{\partial r_k} + [A_{ik} - B_{ik}]\frac{\partial(\underline{\tilde{U}_i} - \underline{\underline{\tilde{U}_i}})}{\partial X_k},
\end{aligned} \tag{A 7}$$

where $A_{ik} = \overline{[\underline{\rho u_i''} - (1/2)(\underline{\rho} + \underline{\underline{\rho}})\underline{u_i''}]\underline{u_k''}}$ and $B_{ik} = \overline{[\underline{\underline{\rho u_i''}} - (1/2)(\underline{\rho} + \underline{\underline{\rho}})\underline{\underline{u_i''}}]\underline{\underline{u_k''}}}$.

https://doi.org/10.1017/jfm.2018.125 Published online by Cambridge University Press

Diffusion term:

$$2\overline{\underline{u}_i'\frac{\partial \underline{\underline{\sigma}}_{ik}'}{\partial \underline{x}_k}} + 2\overline{\underline{\underline{u}}_i'\frac{\partial \underline{\underline{\sigma}}_{ik}'}{\partial \underline{\underline{x}}_k}} - 2\Omega_{ii}(\boldsymbol{x},\boldsymbol{x}') - 2\Omega_{ii}(\boldsymbol{x}',\boldsymbol{x}). \tag{A 8}$$

The diffusion term can be split into pressure, viscous and dissipation components.
Pressure:

$$\begin{aligned} &2\left\{-\overline{\underline{u}_i''\frac{\partial \underline{p}'}{\partial \underline{x}_i}} + \Pi_{ii}(\boldsymbol{x},\boldsymbol{x}') - \overline{\underline{\underline{u}}_i''\frac{\partial \underline{\underline{p}}'}{\partial \underline{\underline{x}}_i}} + \Pi_{ii}(\boldsymbol{x}',\boldsymbol{x})\right\} (\because \overline{X'Y'} = \overline{X''Y'}) \\ &\quad = -\overline{\left\{[1+\underline{\rho}/\underline{\underline{\rho}}]\frac{\partial(\underline{p}'-\underline{\underline{p}}')}{\partial \underline{x}_i} + 2\frac{\partial(\underline{p}'-\underline{\underline{p}}')}{\partial \underline{x}_i}\right\}\underline{u}_i''} \\ &\qquad + \overline{\left\{[1+\underline{\underline{\rho}}/\underline{\rho}]\frac{\partial(\underline{p}'-\underline{\underline{p}}')}{\partial \underline{\underline{x}}_i} + 2\frac{\partial(\underline{p}'-\underline{\underline{p}}')}{\partial \underline{\underline{x}}_i}\right\}\underline{\underline{u}}_i''}. \end{aligned} \tag{A 9}$$

Viscous and dissipation:

$$\begin{aligned} &2\left\{\overline{\underline{u}_i''\frac{\partial \underline{\tau}_{ik}'}{\partial \underline{x}_k}} + E_{ii}(\boldsymbol{x},\boldsymbol{x}') + \overline{\underline{\underline{u}}_i''\frac{\partial \underline{\underline{\tau}}_{ik}'}{\partial \underline{\underline{x}}_k}} + E_{ii}(\boldsymbol{x}',\boldsymbol{x})\right\} (\because \overline{X'Y'} = \overline{X''Y'}) \\ &\quad = 2\left\{\overline{\underbrace{\frac{1}{\underline{\rho}}\left(\underline{\rho}\underline{u}_i'' - \frac{1}{2}[\underline{\rho}+\underline{\underline{\rho}}]\underline{\underline{u}}_i''\right)}_{(\delta u_i)_a}\frac{\partial \underline{\tau}_{ik}'}{\partial \underline{x}_k} - \underbrace{\frac{1}{\underline{\underline{\rho}}}\left(\frac{1}{2}[\underline{\rho}+\underline{\underline{\rho}}]\underline{u}_i'' - \underline{\underline{\rho}}\underline{\underline{u}}_i''\right)}_{(\delta u_i)_b}\frac{\partial \underline{\underline{\tau}}_{ik}'}{\partial \underline{\underline{x}}_k}}\right\} \\ &\quad = \overline{2(\delta u_i'')\left[\frac{\partial \underline{\tau}_{ik}'}{\partial \underline{x}_k} - \frac{\partial \underline{\underline{\tau}}_{ik}'}{\partial \underline{\underline{x}}_k}\right]} + \underbrace{\overline{\frac{\Delta\rho}{\underline{\rho}}\underline{u}_i''\frac{\partial \underline{\tau}_{ik}'}{\partial \underline{x}_k}} - \overline{\frac{\Delta\rho}{\underline{\underline{\rho}}}\underline{u}_i''\frac{\partial \underline{\underline{\tau}}_{ik}'}{\partial \underline{\underline{x}}_k}}}_{\text{VD effects},\mu\Delta\rho} \\ &\quad = \underbrace{\overline{2(\delta u_i')\left[\frac{\partial \underline{\tau}_{ik}'}{\partial \underline{x}_k} - \frac{\partial \underline{\underline{\tau}}_{ik}'}{\partial \underline{\underline{x}}_k}\right]}}_{\text{Density-free}} + \underbrace{\overline{\frac{\Delta\rho}{\underline{\rho}}\underline{u}_i''\frac{\partial \underline{\tau}_{ik}'}{\partial \underline{x}_k}} - \overline{\frac{\Delta\rho}{\underline{\underline{\rho}}}\underline{u}_i''\frac{\partial \underline{\underline{\tau}}_{ik}'}{\partial \underline{\underline{x}}_k}}}_{\text{VD effects},\mu\Delta\rho} (\because \overline{X'Y'} = \overline{X''Y'}), \end{aligned} \tag{A 10}$$

where $(\delta u_i') = \underline{u}_i' - \underline{\underline{u}}_i'$ and we have used the following relationships:

(i) $(\delta u_i)_a = [(\underline{u}_i'' - \underline{\underline{u}}_i'') + (1 - (\underline{\rho}+\underline{\underline{\rho}})/2\underline{\rho})\underline{u}_i''] = [\delta u_i'' + (\Delta\rho/2\underline{\rho})\underline{u}_i'']$, $\delta u_i'' = \underline{u}_i'' - \underline{\underline{u}}_i''$ and $\Delta\rho = \underline{\rho} - \underline{\underline{\rho}}$;

(ii) $(\delta u_i)_b = [((\underline{\rho}+\underline{\underline{\rho}}/2\underline{\underline{\rho}}) - 1)\underline{u}_i'' + (\underline{u}_i'' - \underline{\underline{u}}_i'')] = [\delta u_i'' + (\Delta\rho/2\underline{\underline{\rho}})\underline{u}_i'']$.

Now, the density-free (first) term admits the usual D_ν, $D_{X,\nu}$ and $4\overline{\epsilon}$ terms appearing in the constant-density K–H–M equation (2.1),

https://doi.org/10.1017/jfm.2018.125 Published online by Cambridge University Press

$$\underbrace{2\overline{(\delta u_i')\left[\frac{\partial \tau_{ik}'}{\partial \underline{x}_k}-\frac{\partial \tau_{ik}'}{\partial \underline{\underline{x}}_k}\right]}}_{\text{Density-free}} = 2\mu\left\{\overline{(\delta u_i')\frac{\partial^2(\underline{u}_i'-\underline{\underline{u}}_i')}{\partial \underline{x}_k^2}+(\delta u_i')\frac{\partial^2(\underline{u}_i'-\underline{\underline{u}}_i')}{\partial \underline{\underline{x}}_k^2}}\right\}\ (\mu=\text{const.})$$

$$= \underbrace{2\mu\left\{\overline{\frac{\partial}{\partial \underline{x}_k}\left[(\delta u_i')\frac{\partial(\underline{u}_i'-\underline{\underline{u}}_i')}{\partial \underline{x}_k}\right]+\frac{\partial}{\partial \underline{\underline{x}}_k}\left[(\delta u_i')\frac{\partial(\underline{u}_i'-\underline{\underline{u}}_i')}{\partial \underline{\underline{x}}_k}\right]}\right\}}_{\text{Viscous diffusion},D_\nu+D_{X,\nu}}$$

$$\underbrace{-\,2\mu\left\{\overline{\left(\frac{\partial \underline{u}_i'}{\partial \underline{x}_k}\right)\left(\frac{\partial \underline{u}_i'}{\partial \underline{x}_k}\right)}+\overline{\left(\frac{\partial \underline{\underline{u}}_i'}{\partial \underline{\underline{x}}_k}\right)\left(\frac{\partial \underline{\underline{u}}_i'}{\partial \underline{\underline{x}}_k}\right)}\right\}}_{\text{Dissipation},4\overline{\epsilon}}. \tag{A 11}$$

The second term represents VD effects and vanishes when the density is a constant. Further, $\Delta\rho\to 0$ as $\boldsymbol{x}\to\boldsymbol{x}'$; (A 10) is then determined by the density-free (first) term. This supports the discussions on (2.9).

By setting $\rho=$ constant, all of the terms just derived reduce to their corresponding forms in the constant-density version of the K–H–M equation. The remaining part of this appendix deals with the extra terms that arise due to VDs; these include terms involving the mass flux a_i and terms involving T_{ij} and Q_i.

Mass-flux term:

$$-2\underline{a}_i\frac{\partial\overline{\sigma_{ik}}}{\partial \underline{x}_k}-2\underline{\underline{a}}_i\frac{\partial\overline{\sigma_{ik}}}{\partial \underline{\underline{x}}_k}+2a_i(\boldsymbol{x},\boldsymbol{x}')\frac{\partial\overline{\sigma_{ik}}}{\partial \underline{\underline{x}}_k}+2a_i(\boldsymbol{x}',\boldsymbol{x})\frac{\partial\overline{\sigma_{ik}}}{\partial \underline{x}_k}$$

$$=-2\{\underline{a}_i-a_i(\boldsymbol{x}',\boldsymbol{x})\}\frac{\partial\overline{\sigma_{ik}}}{\partial \underline{x}_k}-2\{\underline{\underline{a}}_i-a_i(\boldsymbol{x},\boldsymbol{x}')\}\frac{\partial\overline{\sigma_{ik}}}{\partial \underline{\underline{x}}_k}$$

$$=\underbrace{2\{\underline{a}_i-a_i(\boldsymbol{x}',\boldsymbol{x})\}\frac{\partial\overline{P}}{\partial \underline{x}_i}+2\{\underline{\underline{a}}_i-a_i(\boldsymbol{x},\boldsymbol{x}')\}\frac{\partial\overline{P}}{\partial \underline{\underline{x}}_i}}_{\text{Mass-flux–pressure}}$$

$$\underbrace{-\,2\{\underline{a}_i-a_i(\boldsymbol{x}',\boldsymbol{x})\}\frac{\partial\overline{\tau_{ik}}}{\partial \underline{x}_k}-2\{\underline{\underline{a}}_i-a_i(\boldsymbol{x},\boldsymbol{x}')\}\frac{\partial\overline{\tau_{ik}}}{\partial \underline{\underline{x}}_k}}_{\text{Mass-flux–stress}}. \tag{A 12}$$

There is no easy way to recast these two terms into the scale space $(\boldsymbol{X},\boldsymbol{r})$, so their forms in the physical space are retained here.

The T_{ii}, Q_i term:

$$\underbrace{\{T_{ii}(\boldsymbol{x},\boldsymbol{x}')+T_{ii}(\boldsymbol{x}',\boldsymbol{x})\}}_{T_{VD}}+\underbrace{2\left\{\frac{Q_i(\boldsymbol{x},\boldsymbol{x}')}{\underline{\rho}}\frac{\partial R_{ik}}{\partial \underline{\underline{x}}_k}+\frac{Q_i(\boldsymbol{x}',\boldsymbol{x})}{\underline{\rho}}\frac{\partial R_{ik}}{\partial \underline{x}_k}\right\}}_{Q}. \tag{A 13}$$

The T term should be zero since the instantaneous velocities are incompressible. The Q term also vanishes in constant-density flows since $Q_i(\boldsymbol{x},\boldsymbol{x}')=(\overline{\rho(\boldsymbol{x}')u_i''(\boldsymbol{x})})/2=(\rho\overline{u_i'})/2=0$.

https://doi.org/10.1017/jfm.2018.125 Published online by Cambridge University Press

Finally, the K–H–M equation for VD flows, of which the constant-density version is its special case, is written below, with $\delta u_i'' = \underline{u_i''} - \underline{\underline{u_i''}}$ and $\delta \tilde{U}_i = \underline{\tilde{U}_i} - \underline{\underline{\tilde{U}_i}}$.

$$
\begin{aligned}
&\frac{\partial \overline{(\delta u_i'')^2_\rho}}{\partial t} + \overbrace{\frac{(\underline{\tilde{U}_k} + \underline{\underline{\tilde{U}_k}})}{2} \frac{\partial \overline{(\delta u_i'')^2_\rho}}}^{\text{Advection},A} + \overbrace{\frac{\partial \overline{\delta u_k'' (\delta u_i'')^2_\rho}}{\partial r_k}}^{\text{Nonlinear transport},\Pi} + \overbrace{\frac{\partial \overline{\delta \tilde{U}_k (\delta u_i'')^2_\rho}}{\partial r_k}}^{\text{Linear transport},\Pi_U} \\
&= \overbrace{-2[A_{ik} + B_{ik}] \frac{\partial \delta \tilde{U}_i}{\partial r_k} - [A_{ik} - B_{ik}] \frac{\partial \delta \tilde{U}_i}{\partial X_k}}^{\text{Production},P} - \overbrace{\frac{1}{2} \frac{\partial \overline{(\underline{u_k''} + \underline{\underline{u_k''}})(\delta u_i'')^2_\rho}}{\partial X_k}}^{\text{Turbulent transport},T} \\
&\overbrace{- \left\{ \overline{[1 + \underline{\rho}/\underline{\rho}] \frac{\partial (\underline{p'} - \underline{p'})}{\partial \underline{x_i}} + 2 \frac{\partial (\underline{p'} - \underline{p'})}{\partial \underline{x_i}} \right\} \underline{u_i''}} + \overline{\left\{ [1 + \underline{\rho}/\underline{\rho}] \frac{\partial (\underline{p'} - \underline{p'})}{\partial \underline{x_i}} + 2 \frac{\partial (\underline{p'} - \underline{p'})}{\partial \underline{x_i}} \right\} \underline{\underline{u_i''}}}}^{\text{Pressure transport},T_p} \\
&\overbrace{+ 2\mu \left\{ \overline{\frac{\partial}{\partial \underline{x_k}} \left[(\delta u_i') \frac{\partial (\underline{u_i'} - \underline{\underline{u_i'}})}{\partial \underline{x_k}} \right]} + \overline{\frac{\partial}{\partial \underline{\underline{x_k}}} \left[(\delta u_i') \frac{\partial (\underline{u_i'} - \underline{\underline{u_i'}})}{\partial \underline{\underline{x_k}}} \right]} \right\}}^{\text{Viscous diffusion},D_\nu + D_{X,\nu}} \\
&\overbrace{- 2\mu \left\{ \overline{\left(\frac{\partial \underline{u_i'}}{\partial \underline{x_k}} \right) \left(\frac{\partial \underline{u_i'}}{\partial \underline{x_k}} \right)} + \overline{\left(\frac{\partial \underline{\underline{u_i'}}}{\partial \underline{\underline{x_k}}} \right) \left(\frac{\partial \underline{\underline{u_i'}}}{\partial \underline{\underline{x_k}}} \right)} \right\}}^{\text{Dissipation},4\overline{\epsilon}} + \underbrace{\overline{\frac{\Delta \rho}{\underline{\rho}} \underline{u_i''} \frac{\partial \underline{\tau_{ik}'}}{\partial \underline{x_k}}} - \overline{\frac{\Delta \rho}{\underline{\rho}} \underline{u_i''} \frac{\partial \underline{\underline{\tau_{ik}'}}}{\partial \underline{\underline{x_k}}}}}_{\text{VD effects},\mu \Delta \rho} \\
&\underbrace{+ 2\{\underline{a_i} - a_i(\boldsymbol{x}', \boldsymbol{x})\} \frac{\partial \overline{P}}{\partial \underline{x_i}} + 2\{\underline{\underline{a_i}} - a_i(\boldsymbol{x}, \boldsymbol{x}')\} \frac{\partial \overline{\underline{P}}}{\partial \underline{\underline{x_i}}}}_{\text{Mass-flux–pressure},a_P} \\
&\underbrace{- 2\{\underline{a_i} - a_i(\boldsymbol{x}', \boldsymbol{x})\} \frac{\partial \overline{\tau_{ik}}}{\partial \underline{x_k}} - 2\{\underline{\underline{a_i}} - a_i(\boldsymbol{x}, \boldsymbol{x}')\} \frac{\partial \overline{\underline{\tau_{ik}}}}{\partial \underline{\underline{x_k}}}}_{\text{Mass-flux–stress},a_\tau} \\
&\underbrace{- \{T_{ii}(\boldsymbol{x}, \boldsymbol{x}') + T_{ii}(\boldsymbol{x}', \boldsymbol{x})\}}_{T_{VD}} \underbrace{- 2 \left\{ \frac{Q_i(\boldsymbol{x}, \boldsymbol{x}')}{\underline{\overline{\rho}}} \frac{\partial \underline{\underline{R_{ik}}}}{\partial \underline{\underline{x_k}}} + \frac{Q_i(\boldsymbol{x}', \boldsymbol{x})}{\underline{\overline{\rho}}} \frac{\partial \underline{R_{ik}}}{\partial \underline{x_k}} \right\}}_{Q}. \qquad \text{(A 14)}
\end{aligned}
$$

Only the first nine terms (A 4)–(A 10) appear in constant-density flows, and each of them is written using the terminology of Valente & Vassilicos (2014). The terms due to VD effects are $\mu \Delta \rho$, a_P, a_τ, T_{VD} and Q.

REFERENCES

Aivalis, K. G., Sreenivasan, K. R., Tsuji, Y., Klewicki, J. & Biltoft, C. A. 2002 Temperature structure functions for air flow over moderately heated ground. *Phys. Fluids* **14**, 2439–2446.

Alves Portela, F., Papadakis, G. & Vassilicos, J. C. 2017 The turbulence cascade in the near wake of a square prism. *J. Fluid Mech.* **825**, 315–352.

https://doi.org/10.1017/jfm.2018.125 Published online by Cambridge University Press

ANTONIA, R. A. & BURATTINI, P. 2006 Approach to the 4/5 law in homogeneous isotropic turbulence. *J. Fluid Mech.* **550**, 175–184.

BURATTINI, P., ANTONIA, R. A. & DANAILA, L. 2005 Scale-by-scale energy budget on the axis of a turbulent round jet. *J. Turbul.* **6**, 1–11.

CARDESA, J. I., VELA-MARTIN, A. & JIMENEZ, J. 2017 The turbulent cascade in five dimensions. *Science* **357**, 782–784.

CASCIOLA, C. M., GUALTIERI, P., BENZI, R. & PIVA, R. 2003 Scale-by-scale budget and similarity laws for shear turbulence. *J. Fluid Mech.* **476**, 105–114.

CHARONKO, J. J. & PRESTRIDGE, K. 2017 Variable density mixing in turbulent jets with coflow. *J. Fluid Mech.* **825**, 887–921.

CHASSAING, P., ANTONIA, R. A., ANSELMET, F., JOLY, L. & SARKAR, S. 2002 *Variable Density Fluid Turbulence, Fluid Mechanics and its Applications*, vol. 69. Springer.

CHASSAING, P., HARRAN, G. & JOLY, L. 1994 Density fluctuation correlations in free turbulent binary mixing. *J. Fluid Mech.* **279**, 239–278.

CHEN, J., MENEVEAU, C. & KATZ, J. 2006 Scale interactions of turbulence subjected to a straining–relaxation–destraining cycle. *J. Fluid Mech.* **562**, 123–150.

CLARK, T. T. 2015. Viscous and diffusive corrections to a Reynolds transport model. *Tech. Rep.* Dept. Mech. Engrg., The University of New Mexico.

CLARK, T. T. & SPITZ, P. B. 2005 Two-point correlation equations for variable density turbulence. *Tech. Rep.* LA-12671-MS. Los Alamos National Laboratory.

DANAILA, L., ANTONIA, R. A & BURATTINI, P. 2004 Progress in studying small-scale turbulence using 'exact' two-point equations. *New J. Phys.* **6**, 128.

DAVIDSON, P. A. 2015 *Turbulence – An Introduction for Scientists and Engineers*, 2nd edn. Oxford University Press.

DIMOTAKIS, P. E. 1986 Two-dimensional shear-layer entrainment. *AIAA J.* **24** (11), 1791–1796.

FUKAYAMA, D., OYAMADA, T., NAKANO, T., GOTOH, T. & YAMAMOTO, K. 2000 Longitudinal structure functions in decaying and forced turbulence. *J. Phys. Soc. Japan* **69**, 701–715.

GAGNE, Y., CASTAING, B., BAUDET, B. & MALECOT, Y. 2004 Reynolds number dependence of third-order velocity structure functions. *Phys. Fluids* **16**, 482–485.

GANAPATHISUBRAMANI, B., LAKSHMINARASIMHAN, K. & CLEMENS, N. T. 2007 Determination of complete velocity gradient tensor by using cinematographic stereoscopic PIV in a turbulent jet. *Exp. Fluids* **42**, 923–939.

GOMES-FERNANDES, R., GANAPATHISUBRAMANI, B. & VASSILICOS, J. C. 2015 The energy cascade in near-field non-homogeneous non-isotropic turbulence. *J. Fluid Mech.* **771**, 676–705.

GOTOH, T., FUKAYAMA, D. & NAKANO, T. 2002 Velocity field statistics in homogeneous steady turbulence obtained using a high-resolution direct numerical simulation. *Phys. Fluids* **14**, 1065–1081.

GUALTIERI, P., CASCIOLA, C. M., BENZI, R. & PIVA, R. 2007 Preservation of statistical properties in large-eddy simulation of shear turbulence. *J. Fluid Mech.* **592**, 471–494.

GUALTIERI, P. & MENEVEAU, C. 2010 Direct numerical simulations of turbulence subjected to a straining and destraining cycle. *Phys. Fluids* **22**, 065104.

HILL, R. J. 2002 Exact second-order structure-function relationships. *J. Fluid Mech.* **468**, 317–326.

VON KÀRMÀN, T. & HOWARTH, L. 1938 On the statistical theory of isotropic turbulence. *Proc. R. Soc. Lond.* A **164** (917), 192–215.

KHOLMYANSKY, M. & TSINOBER, A. 2008 Kolmogorov 4/5 law, nonlocality, and sweeping decorrelation hypothesis. *Phys. Fluids* **20**, 041704.

KOLMOGOROV, A. N. 1941 The local structure of turbulence in incompressible viscous fluid for very large Reynolds numbers. *Dokl. Akad. Nauk. SSSR* **30**, 299–303.

LAVOIE, P., DJENIDI, L. & ANTONIA, R. A. 2007 Effects of initial conditions in decaying turbulence generated by passive grids. *J. Fluid Mech.* **585**, 395–420.

LEE, J. H. W. & CHU, V. H. 2003 *Turbulent Jets and Plumes – A Lagrangian Approach*. Kluwer Publisher.

LÉVÊQUE, E., TOSCHI, F., SHAO, L. & BERTOGLIO, J.-P. 2007 Shear-improved Smagorinsky model for large-eddy simulation of wall-bounded turbulent flows. *J. Fluid Mech.* **570**, 491–502.

https://doi.org/10.1017/jfm.2018.125 Published online by Cambridge University Press

LIBERZON, A., LÜTHI, B., GUALA, M., KINZELBACH, W. & TSINOBER, A. 2005 Experimental study of the structure of flow regions with negative turbulent kinetic energy production in confined three-dimensional shear flows with and without buoyancy. *Phys. Fluids* **17**, 095110.

LIVESCU, D. & RISTORCELLI, J. R. 2007 Buoyancy-driven variable-density turbulence. *J. Fluid Mech.* **591**, 43–71.

LIVESCU, D., RISTORCELLI, J. R., PETERSON, M. R. & GORE, R. A. 2010 New phenomena in variable-density Rayleigh–Taylor turbulence. *Phys. Scr.* **T142**, 014015.

LUMLEY, J. L. 1979 Computational modeling of turbulent flows. *Adv. Appl. Mech.* **18**, 123–176.

MARATI, N., CASCIOLA, C. M. & PIVA, R. 2004 Energy cascade and spatial fluxes in wall turbulence. *J. Fluid Mech.* **521**, 191–215.

MENEVEAU, C. & KATZ, J. 2000 Scale-invariance and turbulence models for lage-eddy simulation. *Annu. Rev. Fluid Mech.* **32**, 1–32.

MOISY, F., TABELING, P. & WILLAIME, H. 1999 Kolmogorov equation in a fully developed turbulence experiment. *Phys. Rev. Lett.* **82**, 3994–3997.

MONIN, A. S. & YAGLOM, A. M. 1975 *Statistical Fluid Mechanics*. vol. II. MIT Press.

MOSER, R. D., KIM, J. & MANSOUR, N. N. 1999 Direct numerical simulation of turbulent channel flow up to $Re_\tau = 590$. *Phys. Fluids* **11** (4), 943–945.

POPE, S. B. 2000 *Turbulent Flows*. Cambridge University Press.

RASMUSSEN, H. O. 1999 A new proof of Kolmogorov's 4/5-law. *Phys. Fluids* **11** (11), 3495–3498.

SADEGHI, H., LAVOIE, P. & POLLARD, A. 2015 Equilibrium similarity solution of the turbulent transport equation along the centreline of a round jet. *J. Fluid Mech.* **772**, 740–755.

SADEGHI, H., LAVOIE, P. & POLLARD, A. 2016 Scale-by-scale budget equation and its self-preservation in the shear-layer of a free round jet. *Intl J. Heat Fluid Flow* **61**, 85–95.

SHEN, X. & WARHAFT, Z. 2000 The anisotropy of the small scale structure in high Reynolds number ($r_\lambda \sim 1000$) turbulent shear flow. *Phys. Fluids* **12** (11), 2976–2989.

TANAKA, T. & EATON, J. K. 2007 A correction method for measuring turbulence kinetic energy dissipation rate by PIV. *Exp. Fluids* **42** (6), 893–902.

TAUB, G., LEE, H., BALACHANDAR, S. & SHERIF, S. 2013 A direct numerical simulation study of high order statistics in a turbulent round jet. *Phys. Fluids* **25**, 115102.

TAYLOR, G. I. 1935 Statistical theory of turbulence. *Proc. R. Soc. Lond.* A **151** (873), 421–444.

THIESSET, F., ANTONIA, R. A. & DANAILA, L. 2013 Scale-by-scale turbulent energy budget in the intermediate wake of two-dimensional generators. *Phys. Fluids* **25**, 115105.

TSINOBER, A. 2009 *An Informal Conceptual Introduction to Turbulence*, 2nd edn. Springer.

VALENTE, P. C. & VASSILICOS, J. C. 2014 The non-equilibrium region of grid-generated decaying turbulence. *J. Fluid Mech.* **744**, 5–37.

VALENTE, P. C. & VASSILICOS, J. C. 2015 The energy cascade in grid-generated non-equilibrium decaying turbulence. *Phys. Fluids* **27**, 045103.

VAN DE WATER, W. & HERWEIJER, J. A. 1999 High-order structure functions of turbulence. *J. Fluid Mech.* **387**, 3–37.

VOIVENEL, L., DANAILA, L., VAREA, E., RENOU, B. & CAZALENS, M. 2016 On the similiarity of variable viscosity flows. *Phys. Scr.* **91**, 084007.

WARHAFT, Z. 2009 Why we need experiments at high Reynolds numbers. *Fluid Dyn. Res.* **41**, 021401.

ZHOU, T. & ANTONIA, R. A. 2000 Reynolds number dependence of the small-scale structure of grid turbulence. *J. Fluid Mech.* **406**, 81–107.

https://doi.org/10.1017/jfm.2018.125 Published online by Cambridge University Press